Geophysical Journal International

Geophys. J. Int. (2025) **242,** 1–19
Advance Access publication 2025 July 16
Research Paper

https://doi.org/10.1093/gji/ggaf178

Seismic waves generated by explosions in, and above, saturated sediments: the Foulness seismoacoustic coupling trials

David N. Green [1], Stuart E. J. Nippress [1], Andy Nowacki,[2] Roger A. Clark,[2] Evie Read,[3] Tuğçe Can Postacı,[2,*] Chris Tilbury,[4] Nick Benson,[3] Sjoerd A. L. de Ridder [2], James Wookey,[3] Nicholas A. Teanby[3] and Barry Stone[4]

[1] *AWE Blacknest, Brimpton, Reading, RG7 4RS, UK. E-mail: dgreen@blacknest.gov.uk*
[2] *School of Earth and Environment, University of Leeds, Woodhouse Lane, Leeds, LS2 9JT, UK*
[3] *Department of Earth Sciences, University of Bristol, Wills Memorial Building, Queens Road, Bristol, BS8 1RJ, UK*
[4] *Spurpark Ltd., Shoeburyness, Essex, SS3 9XE, UK*

Accepted 2025 May 12. Received 2025 May 12; in original form 2025 January 13

SUMMARY

Seismic signals generated by near-surface explosions, with sources including industrial accidents and terrorism, are often analysed to assist post-detonation forensic characterization efforts such as estimating explosive yield. Explosively generated seismic displacements are a function of, amongst other factors: the source-to-receiver distance, the explosive yield, the height-of-burst or depth-of-burial of the source and the geological material at the detonation site. Recent experiments in the United States, focusing on ground motion recordings at distances of < 15 km from explosive trials, have resulted in empirical models for predicting *P*-wave displacements generated by explosions in and above hard rock (granite, limestone), dry alluvium, and water. To extend these models to include sources within and above saturated sediments we conducted eight explosions at Foulness, Essex, UK, where ~ 150 m thicknesses of alluvium and clay overlie chalk. These shots, named the Foulness Seismoacoustic Coupling Trials (FSCT), had charge masses of 10 and 100 kg TNT equivalent and were emplaced between 2.3 m below and 1.4 m above the ground surface. Initial *P*-wave displacements, recorded between 150 and 7000 m from the explosions, exhibit amplitude variations as a function of distance that depart from a single power-law decay relationship. The layered geology at Foulness causes the propagation path that generates the initial *P*-wave to change as the distance from the source increases, with each path exhibiting different amplitude decay rates as a function of distance. At distances up to 300 m from the source the first arrival is associated with direct propagation through the upper sediments, while beyond 1000 m the initial *P*-waves are refracted returns from deeper structure. At intermediate distances constructive interference occurs between *P*-waves propagating through the upper sediments and those returning from velocity-depth gradients at depths between 100 and 300 m. This generates an increase in displacement amplitude, with a maximum at ~ 800 m from the source. Numerical waveform modelling indicates that observations of the amplitude variations is in part the consequence of high *P*- to *S*-wave velocity ratios within the upper 150 m of saturated sediment, resulting in temporal separation of the *P* and *S* arrivals. We extend a recently developed empirical model formulation to allow for such distance-dependent amplitude variations. Changes in explosive height-of-burst within and above the saturated sediments at Foulness result in large *P*-wave amplitude variations. FSCT surface explosions exhibit *P*-wave displacement amplitudes that are a factor of 22 smaller than coupled explosions at depth, compared to factors of 2.3 and 7.6 reported for dry alluvium and granite, respectively.

*Now at: General Directorate of Mineral Research and Exploration, Department of Geophysical Studies, Ankara, Turkey

Key words: Controlled source seismology; Earthquake monitoring and test-ban treaty verification; Wave propagation.

1 INTRODUCTION

Recordings of explosively generated seismic waves can be used to estimate the yield (or charge mass) of a detonation. Historically, significant effort has been expended in identifying relationships between seismic signal parameters, including amplitudes and associated magnitude estimates, and the yield of underground nuclear test explosions (e.g. Douglas & Marshall 1996).

As seismometer deployments have become more widespread, recordings from smaller conventional explosive sources have become more commonplace. Unlike underground nuclear tests these sources are often close to the surface. Examples include truck bomb detonations (Koper *et al.* 1999, 2002), accidental industrial explosions (Pilger *et al.* 2021; Song *et al.* 2022) and munition storage accidents (Nippress *et al.* 2023). To estimate an explosive yield for such sources, the analyst must account for the partitioning of kinetic explosive energy into seismic waves, damage (e.g. crater formation) and airborne acoustics.

Near-surface explosions generate smaller seismic signals than fully coupled buried explosions with commensurate charge masses (e.g. Khalturin *et al.* 1998). Over the past decade there has been a concerted effort to design, and execute, experiments that allow the variation in seismic coupling as a function of explosive height-of-burst or depth-of-burial to be determined (e.g. Bonner *et al.* 2013a, b). The results have allowed empirical models for seismic displacement to be constructed (e.g. Ford *et al.* 2014, 2021; Templeton *et al.* 2018) and then validated against other data sets (e.g. Pasyanos & Ford 2015; Kim & Pasyanos 2023).

For simplicity, we describe height-of-burst and depth-of-burial variations by one continuous parameter, which we denote HoB, with negative/positive values indicating subsurface/subaerial explosions (following the notation of Templeton *et al.* 2018).

Empirical models for predicting explosively generated initial *P*-wave seismic displacements must account for variations caused by: the distance from the source at which the recording is made, the explosive yield, the explosion HoB and the geological setting in which the explosion and seismic propagation takes place (e.g. Ford *et al.* 2014, 2021). The dependence on geological setting limits the wider applicability, or transportability, of such empirical models. In addition, simplifications such as the assumption of isotropic seismic source radiation are often implicit within the model formulation. When interpreting signals generated by an explosion in a given location, an analyst has to consider the applicability of models validated using trials data collected at a different site.

The field trials data from which the empirical models were built have also illustrated the benefit of multiparameter recordings. With measurements of a single phenomenon (e.g. seismic body waves) it is difficult to distinguish between the effects of variations in HoB and yield. The joint analysis of seismic and airborne acoustic (blast) data has been successful in resolving this parameter trade-off (Ford *et al.* 2014; Williams *et al.* 2021).

Ford *et al.* (2021) report seismic displacement models for three generic rock-type environments: hard (granite, limestone), soft (alluvium, soil) and wet (saturated soil). Little information is given regarding the geological variations as a function of depth at the trial locations, and the specific propagation paths taken by the initial *P*-wave as a function of source-to-receiver distance are not considered. These factors are unimportant in areas of homogeneous geology, where the initial *P*-wave will, at all relevant distances, be a direct wave within the same material as that in which the explosion was detonated. The assumption of direct *P*-wave paths is attractive because signal amplitude decay as a function of distance may be explained by a simple power-law relationship. However, in layered geologies (for example, where sediments overlie bedrock), variations in the path taken by the initial *P*-wave (direct wave, refracted head wave) lead to more complex variations in initial *P*-wave amplitude with distance (e.g. Červený 1966; Banda *et al.* 1982). Therefore, it is important to understand the applicability of empirical seismic displacement models, such as those of Ford *et al.* (2014, 2021), in environments where the initial *P*-wave path changes as a function of distance.

Additionally, the Ford *et al.* (2021) wet-rock model is only constrained by data from the Humming Terrapin trials series, for which the majority of the explosions occurred within or above large ponds at Aberdeen Proving Ground, Maryland, US (Stone 2017). Therefore, questions remain about whether the Ford *et al.* (2021) wet-rock model is applicable to explosions in and above saturated sediment, or whether it should only be used for detonations in and above water.

A series of eight explosions were conducted to address the gap in knowledge regarding *P*-wave amplitude variation, as a function of HoB, for explosions in and above saturated sediment. The trials, conducted on Foulness Island, Essex, UK, and referred to as the Foulness Seismoacoustic Coupling Trials (abbreviated to FSCT) were undertaken within and above saturated alluvium and clays overlying more competent sedimentary rocks (Sections 2 & 3).

In this paper we, have focused upon ground motion recordings at distances of between 20 and 7000 m from the explosions (Section 4). These measurements have increased our understanding of energy partitioning for sources within, and above, soft saturated sediments, and allow comparison to previous results. We utilized numerical modelling to improve our understanding of the initial *P*-wave traveltime and amplitude measurements (Section 5). In particular, the modelling results suggest that observed distance-dependent variations in signal amplitude decay rates can be attributed to the effect of geological layering beneath Foulness Island. These findings have been incorporated into a seismic displacement model (Section 6), based upon that of Ford *et al.* (2021).

2 FOULNESS SEISMOACOUSTIC COUPLING TRIALS

FSCT comprised eight detonations within a 75 m × 75 m area of undisturbed ground (referred to as the shotpad) at a UK Ministry of Defence firing range on Foulness Island, Essex, UK, during October 2021 (Fig. 1, Table 1). The site was chosen due to the > 100 m underlying thicknesses of alluvium and clays, facilitating a HoB experiment in soft saturated sediments. A pre-FSCT reflection and refraction seismic survey was conducted to understand the seismic velocity structure in the vicinity of the shotpad (Collins 2018), and a detailed geological description is provided in Section 3.

The eight explosive charges, referred to as S1 to S8, had equivalent TNT charge masses of 10 kg (S1, S7, S8) and 100 kg (S2 to

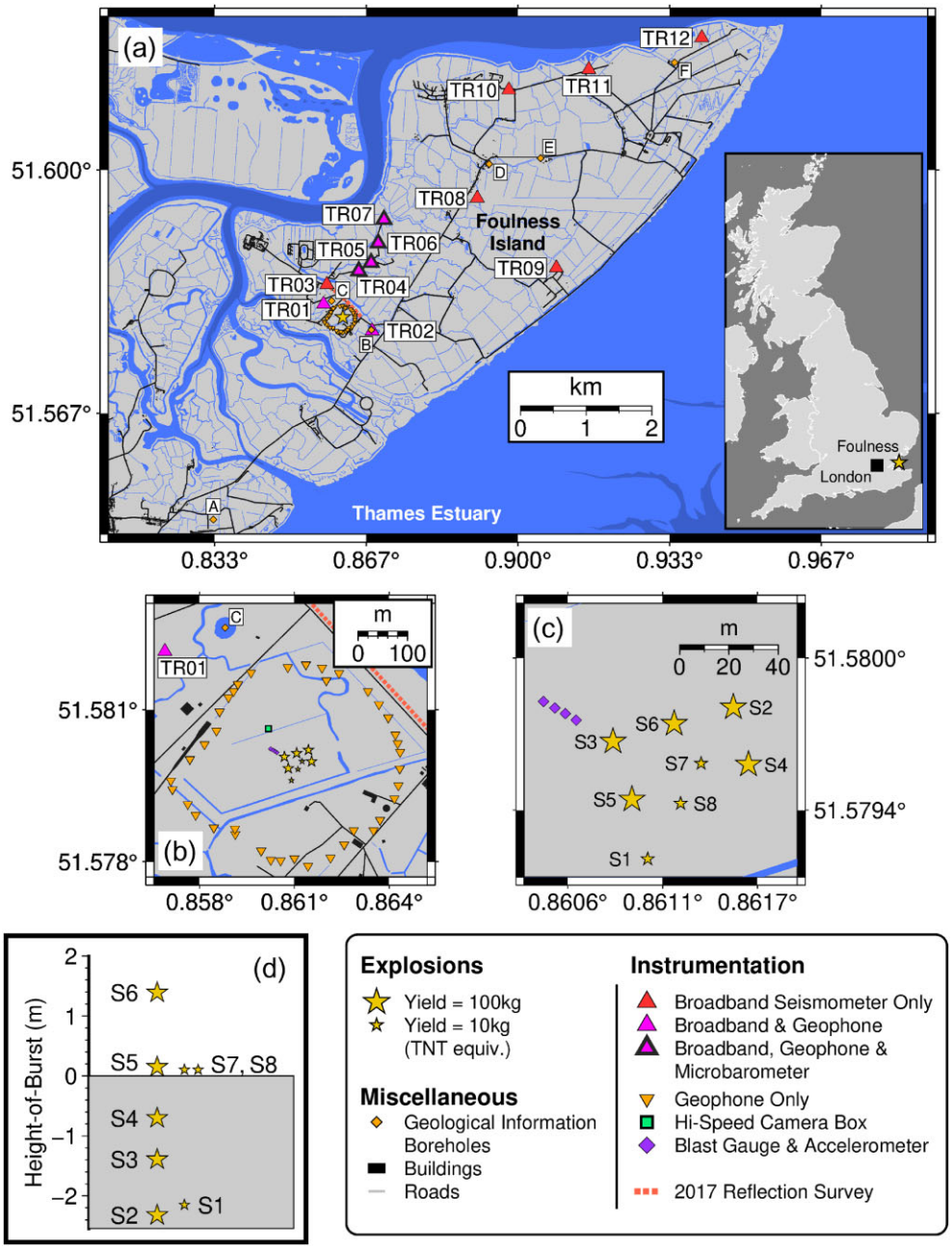

Figure 1. The layout of the FSCT across Foulness Island (panel a), ∼ 70 km east of London (panel a inset). The eight explosions (S1 to S8) were contained within a 75 m × 75 m shotpad, that was surrounded by a ring of geophones (panels b and c). The explosions were detonated at HoB of between 1.4 m above and 2.3 m below the ground surface (panel d, and Table 1). Borehole labels (A to F) correspond to those in Fig. 2. Broad-band seismometer locations are labelled TR01 to TR12.

S6) and were constructed as cylinders to allow emplacement within boreholes. The aspect ratio of the cylinder (1:1.57) was a compromise between requiring a compact source and ensuring a tight fit within the boreholes. The lateral spacing between the explosions across the shotpad (Fig. 1c) was designed to minimize interaction between the explosively generated craters. The allowable FSCT charge mass was restricted by Foulness site regulations, such that the shots were smaller than the explosions underpinning previous empirical models; the distribution of explosive charge masses used in the Ford *et al.* (2021) analysis had a lower quartile to upper quartile range of 91–540 kg.

The explosive package centroid depths were between 2.32 m below the ground surface (S2) and a height of 1.36 m above the ground surface (S6) (Fig. 1d). The above-ground charge (S6) was placed on a wooden platform, and the on-surface explosives (S5, S7, S8) were placed on a thin cardboard sheet. The below-ground explosives (S1 to S4) were emplaced at the base of boreholes, lined using a single length of ribbed high-density polyethylene (HDPE) pipe that ensured the surrounding alluvial sediments did not collapse before charge emplacement. Any small gap (< 100 mm) between the HDPE liner and the edge of the drilled hole was backfilled with sharp sand. Once the charge and cabling were securely

Table 1. Information regarding the eight FSCT trial explosions. W is the TNT equivalent charge mass. Height-of-burst (HoB) values are to the centre of the charge; negative values indicate a buried charge. The positional data was surveyed using 3-D scanning data, combined with a tie-point from satellite imagery, and is consistent with handheld GPS measurements. †: seismic velocities calculated using these times suggest there is a timing discrepancy for these explosions, particularly S8, of up to 0.1 s.

Shot	W (kg)	HoB (m)	Firing time (UTC)	Latitude (°N)	Longitude (°E)
S1	10	−2.15	2021-10-19 10:08:57.226	51.579 266	0.861 024
S2	100	−2.32	2021-10-21 11:19:13.031	51.579 820	0.861 526
S3	100	−1.39	2021-10-20 11:20:50.847	51.579 695	0.860 821
S4	100	−0.70	2021-10-08 10:42:25.936†	51.579 611	0.861 615
S5	100	0.15	2021-10-07 10:59:49.288	51.579 483	0.860 932
S6	100	1.39	2021-10-05 11:30:52.393	51.579 760	0.861 179
S7	10	0.105	2021-10-04 13:57:45.564	51.579 615	0.861 337
S8	10	0.105	2021-10-18 10:49:30.816†	51.579 469	0.861 217

Table 2. Instrumentation deployed during FSCT. N is the number of sensors.

Instrumentation		N	Sampling rate (samples per second)	Distance from shotpad centre (m)	Recording period (2021)
Seismic	Broad-band	12	250	360 to 6950	27-Sep to 25-Oct
	Nodes	46	1000	170 to 1640	27-Sep to 25-Oct
Accelerometers		4	1×10^6	55 to 70	During each explosion
Blast gauges		4	1×10^6	55 to 70	During each explosion
Infrasound		4	100	770 to 1650	28-Sep to 22-Oct
High-speed video		2	10 000 & 2000	95	During each explosion
3-D Scanning		2	–	–	After each explosion

deployed at the base of the borehole, sharp sand was used to stem the borehole to surface level taking care to ensure no voids were present around the charge casing. Further details of the explosives and their emplacement are given in Supporting Information Section A.

An instrumentation suite was deployed across Foulness Island (Fig. 1 and Table 2) to record the seismoacoustic wavefield generated by the FSCT explosions. This paper focuses on seismic data collected at distances of 150 to 7000 m (37 to 1500 m/kg$^{1/3}$ from the 100 kg explosions) for comparison with the models of Ford *et al.* (2014, 2021) alongside closer proximity (< 100 m) accelerometer data that allows comparison with ground shock studies (e.g. Drake & Little 1983). Continuous seismic data, collected across ∼1 month, is available (Green & Nowacki 2021), although not analysed in depth here. Blast wave data, collected on piezoelectric sensors, did not capture the whole low-frequency waveform leading to impulse measurements being underpredicted; an issue identified by Ford *et al.* (2014). However, recorded peak pressures for the above ground shots were consistent with the blast wave model of Kinney & Graham (1985), and the reduction in peak pressure for buried explosions agrees with the observations of Ford & Vorobiev (2023). For completeness this analysis is detailed in Fig.S1 (Supporting Information). High-speed video of the explosions and 3-D laser scans of the resultant craters were also made but have yet to be comprehensively analysed.

3 GEOLOGICAL SETTING

Foulness Island, a ∼ 10 × 4 km area of reclaimed coastal marshland, is located on the northern shore of the Thames Estuary, ∼ 70 km east of London (Fig. 1a inset). The geological sequence underneath the island can, to first order, be described by a six layer model (progressing downward from the surface): Marine and estuarine alluvium (with a thickness of ∼ 20 m), London Clay (∼ 100 m thickness), Lower London Tertiaries (∼ 40 m thickness), Chalk (∼ 200 m thickness), Upper Greensand and Gault Clay (∼ 40 m thickness) underlain by Palaeozoic Basement Sandstones. The upper 200 m of the sedimentary sequence beneath Foulness Island has been constrained from a small number of historical boreholes (e.g. Figs 1a and 2a).

The upper ∼ 20 m at Foulness consists of unconsolidated marine and estuarine alluvium deposits, predominantly formed of clays, silts and sands. Previous studies suggest that the alluvial deposits exhibit P-wave velocities (v_p) of between 1.5 and 1.9 km s^{-1} (Conway *et al.* 1984). Within 500 m of the FSCT shotpad, borehole logs indicate that the alluvium comprises ∼ 8 m of sand overlain by ∼ 9 m of clays and silts (Boshier 1982, 1983, and summarized in Fig. 2a). Undrained triaxial compression tests and consolidation tests indicated that the upper two to three metres of material has a bulk density of between 1.6 and 2.0 Mg m^{-3}. Cohesion (shear strength) values exhibit large variations, but reduce from between 15 and 105 kPa in the desiccated upper layer to between 3 and 10 kPa at depths of 2–3 m. This led Boshier (1983) to conclude that the clays at the depths of the deepest FSCT explosions (∼ 2.3 m) should be classified as very soft.

Beneath the upper alluvial layers lies an ∼ 90 m thickness of London Clay, a unit comprised of silty and sandy clays (e.g. Lake *et al.* 1986); for the purposes of our study we do not attempt to subdivide this into finer lithological units. Across Foulness Island the mapped depth to the base of the London Clay is remarkably consistent, with depths between 103 and 111 m below the surface (Lake *et al.* 1986, and Fig. 2a). London Clay is likely characterized by high v_p/v_s ratios (>5); mean v_p measurements are ∼ 1.6 km s^{-1}, while shear wave velocities (v_s) of between 200 and

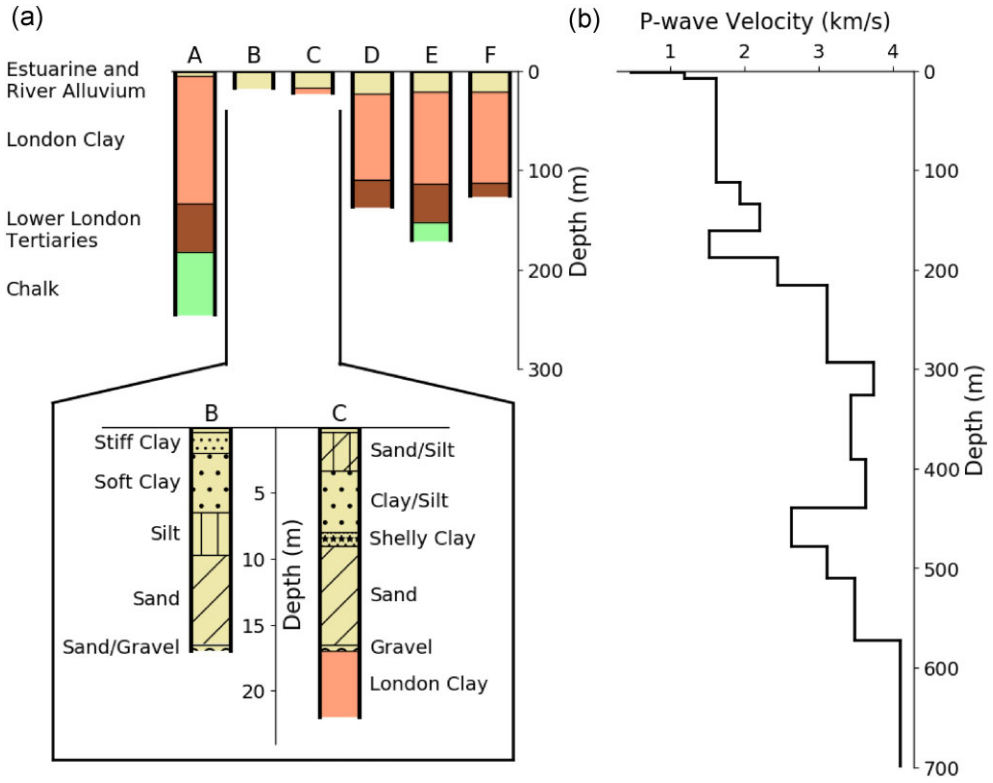

Figure 2. The geological structure beneath Foulness Island (panel a) compared to a *P*-wave seismic velocity profile (panel b) constructed from a seismic reflection survey conducted ~ 300 m to the north–east of the FSCT shotpad (Can 2020). Boreholes labels (A to F) correspond to those shown in Fig. 1(a); boreholes B and C are within 500 m of the FSCT shotpad, and details of the upper 20 m sediment sequence are given at the base of panel (a). Borehole summaries are based upon records provided by British Geological Survey (UKRI).

300 m s^{-1} are reported (e.g. Conway *et al.* 1984; Hight *et al.* 1997; Lessi-Cheimariou *et al.* 2019). Samples of London Clay collected at other UK locations exhibit mechanical anisotropy (e.g. Nishimura *et al.* 2007), but we are unaware of dedicated studies at Foulness and this property is not considered further in this paper.

Below the London Clay lies an ~ 40 m thickness of Palaeogene sediments laid down in a mixture of shallow sea, coastal and fluvial environments (e.g. Sumbler 1996). We refer to these using the historical 'Lower London Tertiaries' classification, rather than splitting the layer into the Lambeth Group (upper ~ 10 m of sands) and Thanet Sand (lower ~ 30 m of clays and sands) due to the low confidence in being able to distinguish between the two in historical borehole records. Seismic investigations of the Lower London Tertiaries at a site ~ 85 km to the north–east of Foulness suggests that shear-wave velocities within this unit are low ($v_s < 500$ m s^{-1}), with the clays of the Thanet Sand perhaps forming a low-velocity zone with v_s as low as 300 m s^{-1} (Hight *et al.* 1997).

Carboniferous chalk deposits underlie the Lower London Tertiaries (Fig. 2a), with the interface at a depth of ~ 160 m (Lake *et al.* 1986). Although the deposit thickness has not been proven via drilling on Foulness Island, deep boreholes across the Thames Estuary region have revealed a relatively consistent 200 $\pm$15 m thickness of chalk. Despite southern UK chalk having variable geomechanical strength properties, related in part to the presence of clay-rich marl beds (e.g. Bell *et al.* 1999), a single layer description is sufficient for our purposes. Beneath the chalk the closest deep borehole, 18 km from the FSCT shotpad, reveals a 40 m thickness of early Cretaceous sandstones and mudstones (the Upper Greensand and Upper Gault) before Palaeozoic sandstones are reached at a depth of ~ 400 m (Smart *et al.* 1964; Lake *et al.* 1986).

A seismic reflection survey, conducted a few hundred metres to the north–east of the FSCT shotpad (see Collins 2018; Can 2020), resulted in a v_p profile (Fig. 2b). This suggests that the sediments in the upper ~ 100 m have v_p values of ~ 1.7 km s^{-1}, with the upper < 10 m likely exhibiting lower v_p of ~ 1.2 km s^{-1}. Below these units, the first-order behaviour is a positive v_p gradient with increasing depth, such that at a depth of ~ 400 m the estimated v_p has increased to between 3.5 and 4.0 km s^{-1}.

4 DATA AND RESULTS

The focus of this paper is to understand better the variability in seismic amplitudes generated by near-surface explosions within saturated sediment environments, and the influence of layered geological structures upon the observations. In this section, we describe the analysis methodologies applied to, and results gained from, FSCT ground motion data collected on (i) accelerometers at distances < 90 m from the explosions and (ii) seismometers located across Foulness Island at distances between 150 and 7000 m from the shotpad.

In studies of explosively generated phenomena, including seismic amplitudes, hydrodynamic scaling relationships are often employed to relate measurements across wide ranges of physical time and length scales (e.g. Ford *et al.* 2021). These scaling laws describe how, for point-source explosions, time and length scale with the cube-root of yield (e.g. Denny & Johnson 1991); cube-root scaling

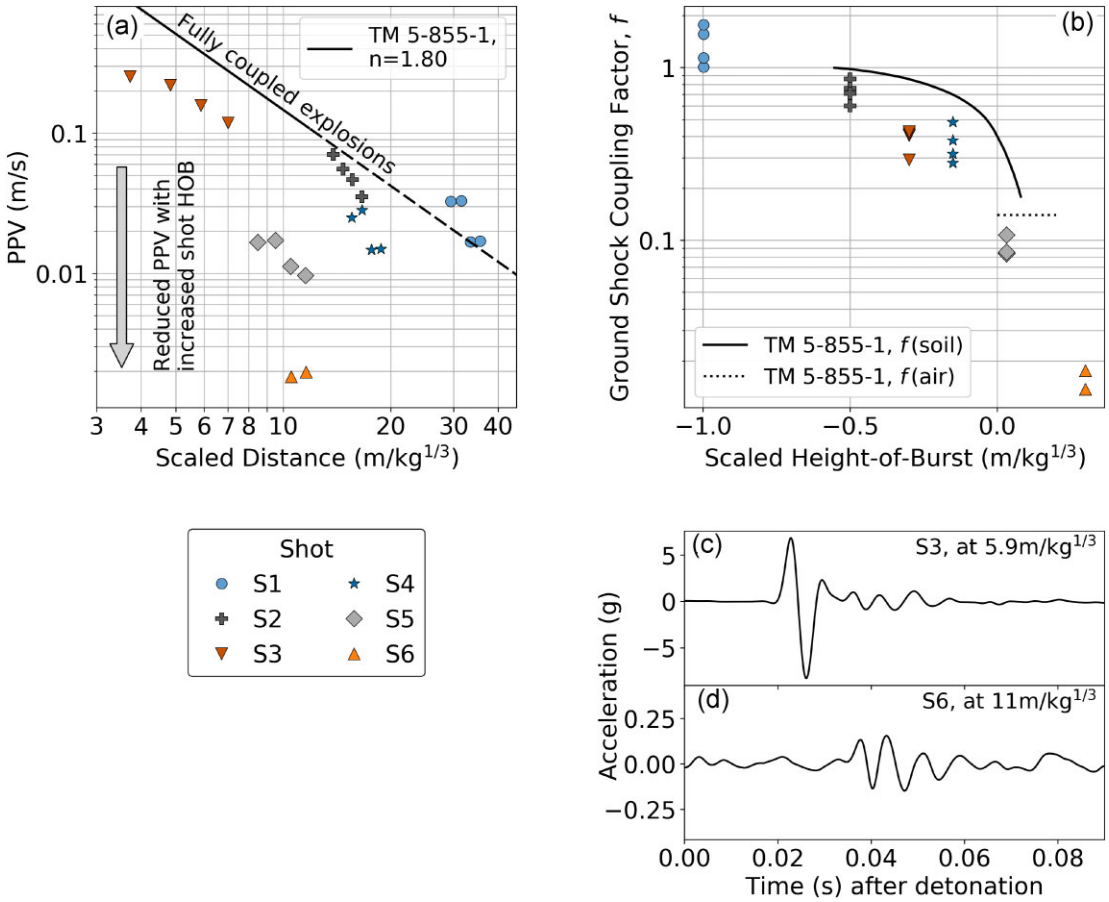

Figure 3. Vertical ground motion measured on accelerometers within 87 m of the FSCT explosions (Fig. 1c). The measured peak particle velocities (PPV) are dependent upon both the scaled distance from the source (panel a) and the height-of-burst (panel b). Only two recordings are available for shot S6. A Department of the Army (1986) model (TM 5-855-1) for ground shock generated PPV for buried explosions has been fit to the S1 and S2 data (panel a, black line: solid in distance range of original TM 5-855-1 study, dashed when extrapolated to further distances). The ground shock coupling factors are illustrated in panel (b); the lines indicate the TM 5-855-1 models ($f(\tilde{h})$, eq. 1) while the data points are the ratio of the measured FSCT PPV to that predicted by the TM 5-855-1 model for a fully coupled explosion (f_{FSCT}, eq. 2). Example acceleration recordings are provided in panels (c) and (d); positive values indicate upwards motion.

has been validated for seismic displacement measurements from near-surface explosions (Templeton *et al.* 2018). Following the notation of Ford *et al.* (2021), we denote scaled variables with an over tilde. For example, the physical source-to-receiver distance is given by r (m), while the scaled distance is $\tilde{r} = rW^{-1/3}$ (m/kg$^{1/3}$) where W is the explosive charge mass, or yield.

4.1 Near-source acceleration recordings

Four Endevco Model 2228C triaxial piezoelectric accelerometers, with a flat response ($\leq$5 per cent deviation) to accelerations between 1 and 4000 Hz, were emplaced at a depth of 0.6 m below the ground surface along a radial line approximately North–West from the centre of the explosives pad (Fig. 1c), such that the distances between detonation and sensor varied between 17 m (for the closest sensor to S3) and 87 m (for the furthest sensor from S4). Recordings were made at 1×10^6 samples per second. Prior to deployment the corners of each sensor were screwed onto the top of a metal rod that was then set into a plaster cube with edge lengths of 100 mm; this cube provided a stable base for the sensor with a density similar to that of the surrounding ground material. Across the weeks of deployment the vertical component recordings proved to be more reliable than the horizontal components, some of which failed likely due to water ingress during the experiment. Therefore, only vertical recordings are considered within this analysis.

The acceleration recordings (e.g. Fig. 3) consist of arrivals that have both propagated through the ground to the station and, for explosions at or above the surface, an air-to-ground coupled phase associated with the later arrival of the blast wave (not shown). The FSCT recordings of the ground propagated wave consist of short (<0.05 s) waveforms with a peak frequency content of between 100 and 200 Hz; they do not exhibit the classic rapid onset and exponential decay of ground shock recordings at very short stand-off distances (e.g. Shelton *et al.* 2014). Across the twenty observations from explosions S1 to S5 the arrival times of the first arrival on the vertical channel is consistent with a propagation velocity of 1.66 $\pm$0.06 km s^{-1} (median value $\pm$ median absolute deviation).

Previous studies of ground motions close to explosions include the Department of the Army (1986) Technical Manual, referred to here as TM 5-855-1, that builds on work by Drake & Little (1983). To compare Foulness recordings with ground velocity relationships in TM 5-855-1, a linear trend was removed from unfiltered FSCT

acceleration recordings prior to integration. The peak particle velocity (PPV) was then measured as the maximum zero-to-peak amplitude on the vertical component recording. PPV values decrease with both distance from the source (Fig. 3a), as expected due to geometric spreading and attenuation, and as the explosive HoB increases. TM 5-855-1 provides empirically derived relationships for expected PPV values close to explosions within various soil types, which in metric units can be expressed as,

$$V_0(\tilde{r}, \tilde{h}, n) = 48.77 f(\tilde{h}) (2.5208\tilde{r})^{-n} \quad (1)$$

where V_0 is the peak particle velocity (m s^{-1}), $\tilde{r}$ is the scaled source-to-receiver distance (m/kg$^{1/3}$), $\tilde{h}$ is the scaled height-of-burst (m/kg$^{1/3}$), $f(\tilde{h})$ is a ground shock coupling factor and n is a geologically dependent coefficient that accounts for geometrical spreading and attenuation. Values of n vary between 1.5 for heavy saturated clays and 3.25 for loose, dry sands.

We fit a TM 5-855-1 model (eq. 1) to the FSCT PPV measurements made within 100 m of the explosions, to confirm they are consistent with previous recordings in, and above, saturated soils. To estimate n for the FSCT data we make the assumption that explosions S1 and S2 are fully coupled, that is, $f = 1$ (the TM 5-855-1 $f(\tilde{h})$ function indicates $f > 0.95$ for the S1 and S2 HoB values). Minimizing the sum of squared residuals between the S1 and S2 PPV observations and the eq. (1) predictions, across a physically reasonable range of n values, results in an estimate of n=1.8 (black line, Fig. 3a). This is consistent with previous measurements in saturated sandy clays. However, it is noted that the calculation has limitations including: (1) the original measurements were made at shorter scaled distances (< 12 m/kg$^{1/3}$) than we have access to at FSCT, and (2) the fit is sensitive to the limited range of scaled distances at which we observe S1 and S2.

To compare to the HoB coupling curve of TM 5-855-1 (i.e. $f(\tilde{h})$) we normalize the Foulness PPV measurements, PPV$_{\text{meas}}$, with respect to the predicted value, PPV$_{\text{pred}}$, for a fully coupled explosion at the measurement distance, taking $n = 1.80$,

$$f_{\text{FSCT}}(\tilde{h}) = \frac{\text{PPV}_{\text{meas}}(\tilde{r}, \tilde{h})}{\text{PPV}_{\text{pred}}(\tilde{r}, \tilde{h}, n)} = \frac{\text{PPV}_{\text{meas}}(\tilde{r}, \tilde{h})}{V_0(\tilde{r}, -1, 1.80)} \quad (2)$$

Once the effect of amplitude decay with distance has been removed, measured PPV values reduce by approximately two orders of magnitude between fully coupled (S1 at $\tilde{h} = -1.0$ m/kg$^{1/3}$) and above ground explosions (S6 at $\tilde{h} = 0.3$ m/kg$^{1/3}$). The calculated $f_{\text{FSCT}}(\tilde{h})$ values exhibit a more gradual reduction in PPV as a function of increasing $\tilde{h}$ when compared to the TM 5-855-1 $f(\tilde{h})$ function (Fig. 3b), which reduces rapidly between $\tilde{h} = -0.1$ and $\tilde{h} = 0.1$ m/kg$^{1/3}$. However, the coupling for a surface explosion (e.g. S5 where the FSCT coupling factor ~0.1) is close to that recommended by TM 5-855-1 for contact bursts ($f = 0.14$).

4.2 Ground velocity recordings across Foulness Island

The FSCT seismic network contained 12 broad-band sensors and 46 geophones (Fig. 1a); all sensors recorded three orthogonal components of motion. The broad-band seismometer network consisted of 10 Güralp Certimus sensors (locations TR01 to TR10) and two Güralp 6TD sensors (locations TR11 and TR12); all broad-band sensors recorded at 250 samples per second. These sensors spanned a distance range of [360, 6960] m from the centre of the FSCT shotpad. The broad-band sensors were deployed upon a metal plate sitting on a bed of compacted damp sand within a sunken barrel, and timing information was provided by an external Global Navigation Satellite System (GNSS) antenna. The geophones (SmartSolo nodes), with a natural frequency of 5 Hz and a flat response to velocity above ~ 10 Hz, recorded at 1000 samples per second (see Figs S2 to S4 in the Supporting Information for a comparison of sensor responses and recorded waveforms). These nodes have an integral GNSS timing unit, and were deployed directly into the soft earth such that the top of the unit was flush with the ground surface (or just below); care was taken to ensure voids were not left around the geophones. During FSCT, 40 nodes were deployed in a ring approximately 200 m from the centre of the shotpad (Fig. 1b) and six were co-located with the broad-band stations closest to the explosions (except TR03). The co-located sensors provided both a comparison with the broad-band recordings and redundancy if the closest broad-band sensors clipped (which they did for the large buried explosions).

The seismic network recorded signals for all eight of the FSCT explosions, with a wavefield composed of multiple body-wave paths, air-to-ground coupled arrivals and surface waves (Figs 4 and 5). Prior to analysis the instrument response was deconvolved from all waveform data, returning velocity seismograms in physical units; this was particularly important to allow direct comparison between geophone and broad-band recordings. Arrival time picks were made manually in two two-octave passbands: [0.5, 5] Hz to allow direct comparison with Ford *et al.* (2014, 2021) and [3, 30] Hz as seismograms in this passband exhibited higher signal-to-noise ratios (while the upper frequency limit remained below the spectral corner frequency of the explosive sources). Only the initial *P*-waves exhibited impulsive arrivals (e.g. Figs 4b and c), while later arrivals were either emergent in nature, or had low-amplitude initial arrivals that were obscured by earlier arriving energy.

4.3 Seismic wavefield overview

Broad-band body wave arrivals were recorded for all explosions, with corner frequencies of ~50 or 70 Hz depending upon source charge mass (see Fig. S5 in the Supporting Information). The body wave amplitudes are a function of charge mass, HoB and propagation distance, with the most deeply buried 100 kg explosion (S2) generating the largest ground motion (e.g. Fig. 4). *P*-wave amplitude measurements are described further in Section 4.4. Recordings on sensors within 400 m of the explosions comprise an initial *P*-wave arrival propagating at ~ 1.7 km s^{-1} followed by a series of coherent reflections from deeper layers (Fig. 5c). At stations beyond ~ 600 m from the source, the initial *P*-wave arrival times are consistent with refractions from deeper layers (Figs 5a and b). Following the initial refracted arrival, a larger amplitude, temporally extended, wave packet propagates at ~ 1.7 km s^{-1} and is interpreted as body wave energy travelling through, and reverberating within, the ~150 to 200 m of soft sediments that overlie the denser chalk (e.g. Fig. 2).

Air-to-ground coupled arrivals, associated with the arrival of the atmospheric air-wave at the station, are observed propagating across the network with velocities of ~ 345 m s^{-1} for both the above surface and near-surface explosions (S3 to S8), with reducing amplitudes as the depth of the explosion increases. For the deepest two explosions (S1 and S2) the air-to-ground arrival is not clearly observed due to a combination of reduced signal amplitude and increased explosion-generated seismic noise (e.g. Fig. 4 for signals at TR06). A Hyperion IFS-3000 microbarometer, co-located with the seismic sensors at TR06, allowed air-to-ground coupling coefficients to be estimated via comparison of time domain peak-to-peak

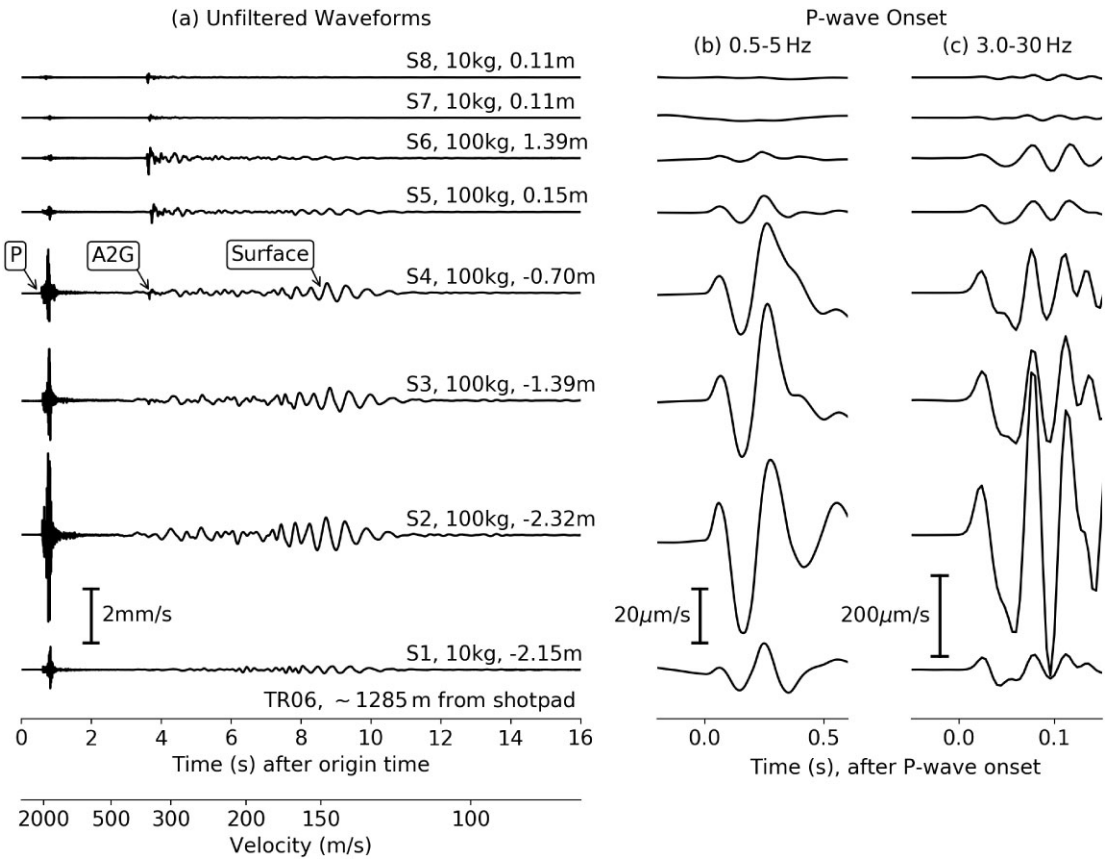

Figure 4. Velocity seismograms recorded at TR06, 1285 m from the centre of the shotpad for the eight explosions (S1 to S8). Labels to the right of panel (a), showing unfiltered waveforms, indicate the explosive charge mass (kg) and HoB (m). Boxed annotations indicate the *P*-wave, air-to-ground coupled (A2G) and surface wave arrivals. Details of the *P*-wave onsets are shown in two passbands: 0.5 to 5 Hz (panel b) and 3.0 to 30 Hz (panel c).

amplitudes. In the 2 to 4 Hz passband the coupling coefficient is estimated to be $\sim 8 \times 10^{-6}$ m s^{-1} Pa^{-1}, consistent with measurements in other areas of low-velocity near-surface sediments (e.g. Wills *et al.* 2022).

A surface wave packet, with energy in the 1–4 Hz passband, arrives after the coupled airwave. For the below ground explosions, this surface wave packet comprises two prominent branches: a lower frequency (1.0–1.5 Hz) normally dispersed branch that starts almost co-incident with the airwave (at a velocity of ~ 350 m s^{-1}) and a higher frequency (1.5–4 Hz) inversely dispersed branch that arrives with a velocity of ~ 180 m s^{-1}. The branches merge to form an Airy phase at a time corresponding to a velocity of 120 m s^{-1}. For the above ground explosions, the surface wave is dominated by an almost monochromatic phase (with a frequency of ~ 1.75 Hz) that again arrives with source-to-station velocities of between 350 and 120 m s^{-1}. Read (2024) provides a detailed study of these surface wave arrivals, and a comparison with previous studies of such phases (e.g. Jardetzky & Press 1952; Langston 2004). An assessment of their amplitude variation (as a function of charge mass, HoB and source-to-receiver distance) will be the subject of a future study.

4.4 Seismic *P*-wave amplitudes

First arrival *P*-wave displacement amplitudes were calculated from bandpass filtered instrument-corrected vertical component velocity seismograms, by integrating across the initial positive velocity pulse following the *P*-wave arrival time pick. The initial *P*-wave pulse was identified as being between the datapoint closest to the *P*-wave arrival time (t_P) and the next datapoint for which the velocity was less than that recorded at t_P. To reduce errors due to the discretization of the seismogram, the recordings were resampled using a Fourier (or sinc) interpolation with a sampling rate of 2000 samples per second; testing showed this resampling did not introduce artifacts into the initial *P*-phase pulse.

In this study, we use vertical-component amplitudes. Ford *et al.* (2021) maximized the initial *P*-wave amplitude by rotating the three-component seismograms using a Principal Component Analysis (PCA) to identify the directional vector onto which to project the seismic waveforms. However, low signal-to-noise ratios in the [0.5, 5] Hz passband at Foulness, particularly on the horizontal components, result in highly variable PCA-optimized amplitudes. In the [3, 30] Hz passband, where root-mean-squared horizontal noise amplitudes have a median value 15 times smaller than in the [0.5, 5] Hz passband, a comparison of vertical and PCA-optimized amplitudes across the network showed that in 90 per cent of cases there was less than 7 per cent difference between the two measurements. This indicates that the initial *P*-waves at Foulness are dominated by vertical motion, and that analysing vertical component amplitudes and comparing to the PCA-optimized amplitudes of Ford *et al.* (2021) is justifiable. The small horizontal signal amplitudes also make an across-network comparison of *P*-wave polarization attributes difficult; we therefore restrict our analysis to vertical recordings.

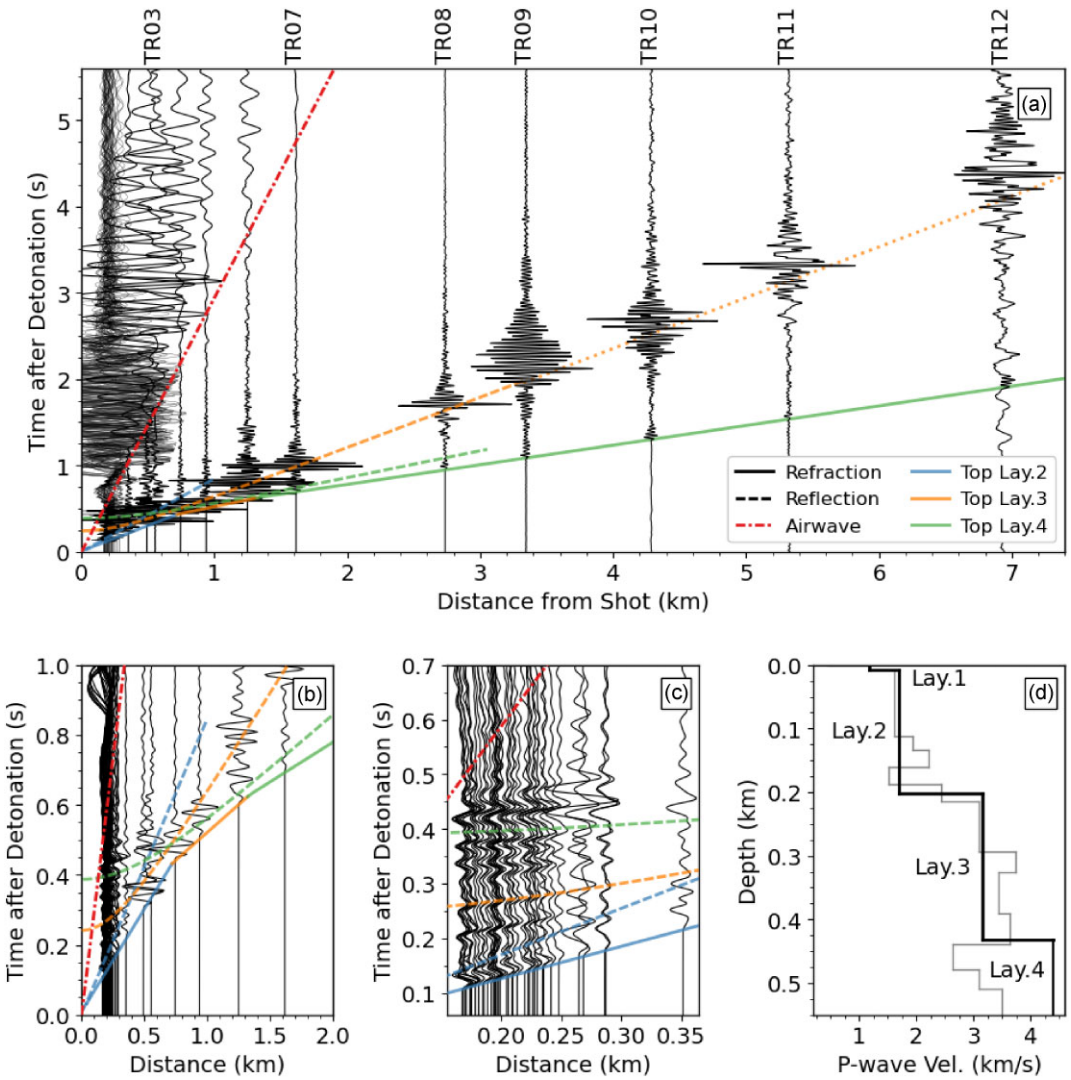

Figure 5. Seismogram record sections, bandpass filtered between 3 and 30 Hz, recorded after explosion S2. The body wave packets that arrive before the airwave are shown in panel (a), with arrivals from ray-tracing through the best-fitting four layer model (black line, panel d) shown as coloured lines. The dotted line that continues the reflected arrival from the top of Layer 3 out to distances greater than ~ 3.5 km represents an arrival with a velocity of 1.7 km s^{-1}, that is, a direct wave though Layer 2. Details of the near-source arrivals, out to distances of 2 km and 350 m, are shown in panels (b) and (c), respectively. The thin grey line in panel (d) is the model of Can (2020).

Displacement amplitudes, d, recorded at Foulness do not decrease with a constant power-law gradient as a function of source-to-receiver distance, r (Figs 6a and b). Measurements across all explosions, and both frequency bands, exhibit a near constant power-law decay gradient at distances < 300 m from the source (i.e. $d \propto r^{-x_1}$) before the amplitudes increase to a maximum and then decay with a different power law exponent as source-to-receiver distance increases (i.e. $d \propto r^{-x_2}$ where $x_2 \neq x_1$).

The power-law gradients, and the source-to-receiver distance and magnitude of the amplitude maximum, are frequency band dependent. In the [0.5, 5] Hz band the amplitude maximum occurs at ~ 1000 m from the source and is only ~33 per cent larger than the amplitude minimum that occurs at a distance of ~ 700 m from the source (Fig. 6a). In contrast, the amplitude maximum for the [3, 30] Hz measurements occurs closer to the source (between distances of 700 and 800 m) and is considerably larger; amplitudes at the maximum are between two and three times larger than those recorded between 300 and 400 m from the source (Fig. 6b). Estimates of the power-law exponents are made during construction of a P-wave amplitude model in Section 6.

We note that the distance at which the amplitudes reach a maximum, and the distance ranges in which particular power-law gradients are applicable, are a function of physical distance not scaled distance (compare, e.g. Figs 6b and d). This is consistent with the amplitude variations with distance being controlled by geometrical propagation effects (e.g. multipathing through layered structures) rather than an effect of the explosive source. This is explored further in Section 6 when considering the appropriate scaling of parameters within empirical models of P-wave displacement.

Hydrodynamic scaling of length variables is required to simplify the relationship between explosive HoB and displacement amplitudes (Fig. 6c), that is, $\tilde{d}$ is a function of $\tilde{h}$ whereas d is not a function of h. For example, although shots S1 (a 10 kg shot at $\tilde{h} = -1.0$ m/kg$^{1/3}$) and S5 (a 100 kg shot at $\tilde{h} = 0.07$ m/kg$^{1/3}$) produce

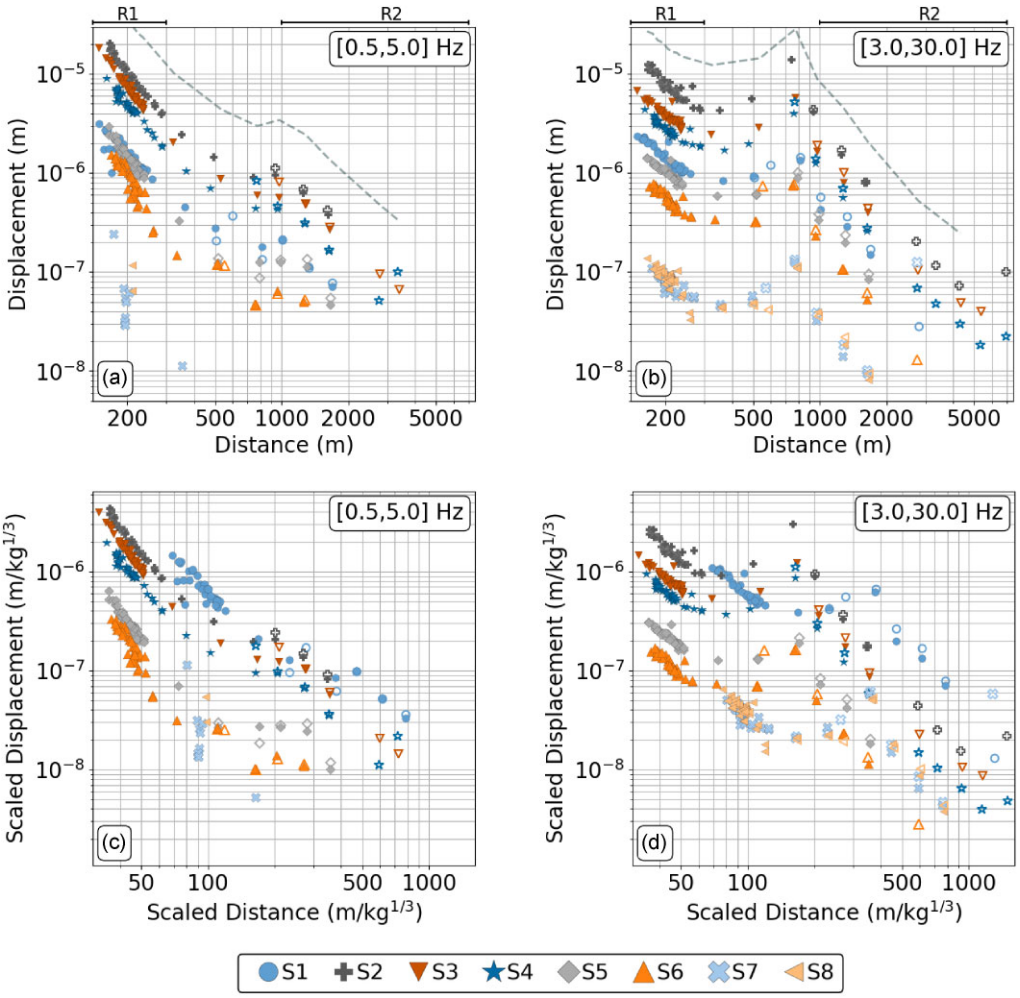

Figure 6. First arrival *P*-wave displacements across the FSCT seismic network, measured in two passbands: [0.5, 5] Hz (panels a and c) and [3, 30] Hz (panels b and d). Filled symbols indicate geophone nodes, open symbols indicate broad-band sensors. R_1 and R_2, shown above panels (a) and (b), refer to the distance ranges in which models of approximately power-law distance decay are fit (Section 6). The grey dashed lines, representing a smoothed fit through the S3 data, are vertically offset from the observed amplitudes and have been added to provide a visual guide to the general form of displacement decay with distance. In panels (c) and (d) the underlying amplitude data are the same as that for panels (a) and (b), respectively; the difference is that the amplitudes and distances in the lower panels have been scaled by the cube-root of the explosive charge mass. A comma separated variable file containing the displacement measurements is provided in the Supporting Information.

comparable displacements (Fig. 6a), S1 exhibits scaled displacements that are a factor of ∼40 greater than those for S5 at a given scaled distance.

To inform our efforts to construct an empirical model for the FSCT seismic displacements, we first employ numerical modelling to identify seismic velocity profiles as a function of depth that can explain the major features of the recorded arrival times and amplitudes.

Table 3. The best-fitting four layer *P*-wave velocity model, constrained using *P*-wave arrival picks and the associated *P*-wave quality factor, Q_p, estimated for the expected materials in these depth ranges.

Thickness (m)	v_p (km s^{-1})	Q_p
7	1.18	5
195	1.70	95
230	3.15	150
Half-space	4.40	200

5 MODELLING THE *P*-WAVE VELOCITY STRUCTURE

The initial *P*-wave arrival time observations across the FSCT seismometer network can, to first order, be split into three distance ranges with approximately constant v_p: [150, 800] m, [800, 1300] m and [1300, 7000] m with the velocity increasing from ∼1.7 to 4.4 km s^{-1} as the distance increases (Fig. 5b). We use FSCT refraction and reflection arrival times to invert for a simple four-layer v_p model, by minimizing the sum of squared residuals between 22 observations and predictions made using the Herrmann (2013) *refmod96* algorithm. Details are provided in Supporting Information Section F and the model, referred to as our baseline four-layer model, is summarized in Table 3.

The observed amplitude variations as a function of source-to-receiver distance (Fig. 6) provide additional information to help constrain models of the subsurface structure. Simulated *P*-wave displacement measurements have been made from waveforms

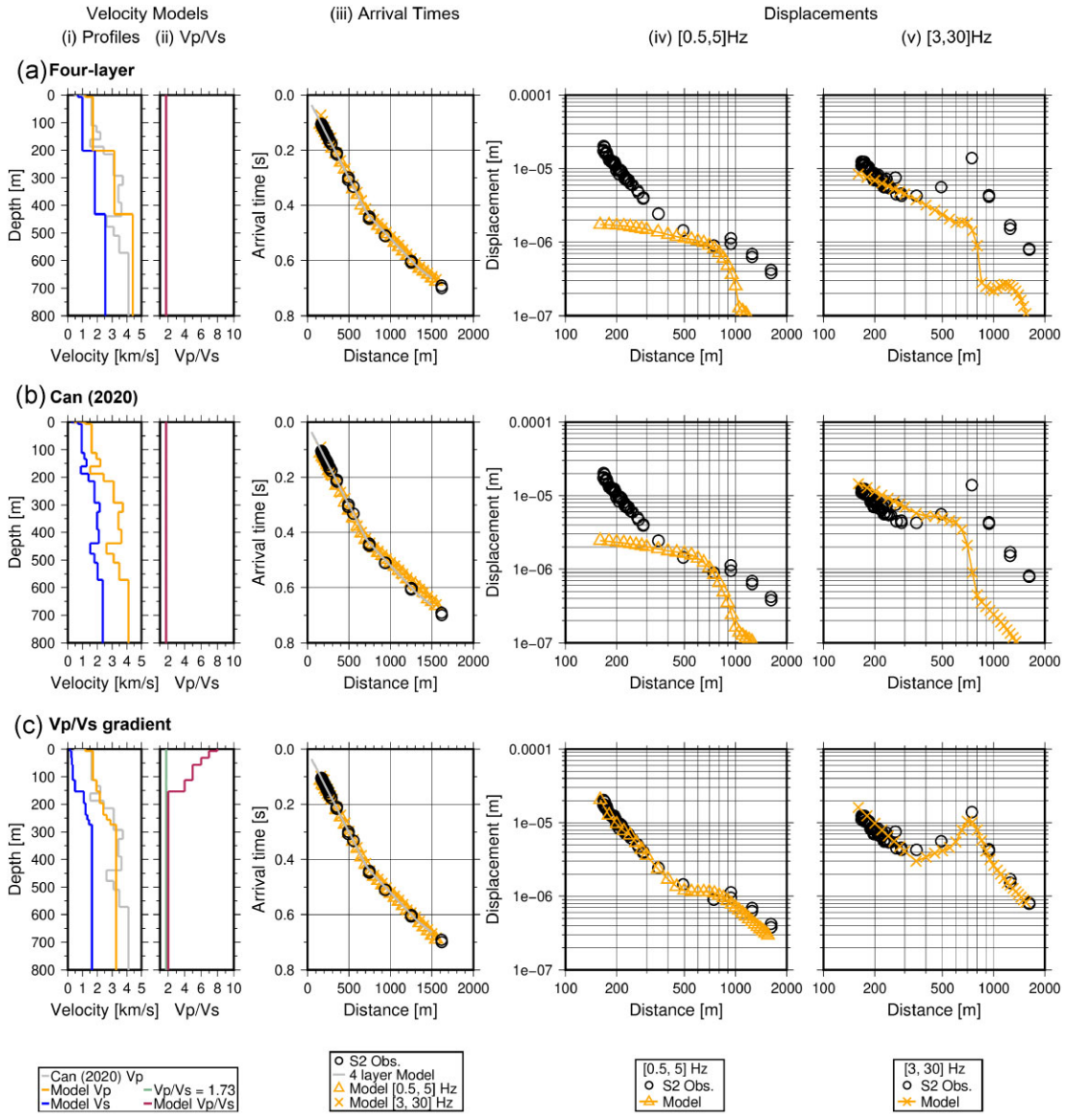

Figure 7. A comparison of arrival time and displacement amplitude observations with numerical modelling results using three simplified seismic velocity models: (a) our baseline four-layer model constrained using arrival time data only (Table 3), (b) the *P*-wave velocity model of Can (2020), with an assumed v_p/v_s ratio of 1.73 and (c) our preferred model where the v_p/v_s ratio is allowed to increase within the upper 200 m. From left to right the five panels for each model give (i) the model v_p and v_s profiles (in orange and blue, respectively) in comparison to the v_p profile estimated by Can (2020) (in grey), (ii) the model v_p/v_s ratio (in maroon) in comparison to a v_p/v_s ratio of 1.73 (in green), (iii) a comparison of the observed and modelled *P*-wave arrival times, and comparisons of the initial *P*-wave amplitudes in comparison to observations for explosion S2 in the (iv) [0.5, 5] Hz and (v) [3, 30] Hz passbands.

generated by propagating a 0.064 s duration parabolic pulse through a suite of velocity models using the Herrmann (2013) wavenumber integration code. This modelling required a simple attenuation model, characterized by the *P*-wave quality factor, Q_p, to be developed for the subsurface. The model is summarized in Table 3, and detailed in Supporting Information Section G. However, tests showed that modelled *P*-wave arrival amplitudes at the frequencies and stand-off distances considered in this study are insensitive to the Q_p values employed. An example of the waveform simulation input is provided in Supporting Information Section H.

Using the baseline four-layer model (Table 3) the initial *P*-wave onsets of the simulated waveforms provide a good fit to the arrival time data as expected, but the simulated *P*-wave amplitudes do not reproduce the observations in either the [0.5, 5] Hz or [3, 30] Hz passbands (Fig. 7a). In the [0.5, 5] Hz passband the simulated *P*-wave amplitudes exhibit a reduced variation with distance compared to the observations. This is due to interference between the initial *P*-wave pulse and a later downward motion, likely an S_v arrival, reducing the amplitude (see Supporting Information Section H for an illustration of this effect). At distances > 1000 m the simulated amplitude reduces rapidly as a low-amplitude refracted arrival from the deepest model layer interface separates from the later arriving wavefield. In the [3, 30] Hz passband the gradient of the simulated amplitude decay at short source-to-receiver distances (< 350 m) is comparable to that observed. The seismic arrival pulse widths in this passband are shorter, such that the *P*- and *S*-waves do not interfere when using a nominal v_p/v_s ratio of 1.73. However, the observed increase in *P*-wave amplitudes at distances of between

∼400 and 1000 m from the source, with a maximum at ∼ 700 m, is not predicted. Reductions in amplitude are observed as refracted waves from successively deeper layers emerge as the initial arrival.

Increasing the model complexity by employing the Can (2020) *P*-wave velocity model (and again assuming $v_p/v_s = 1.73$ throughout) produces simulated waveforms with similar arrival times and amplitude characteristics as the four layer model (Fig. 7b). At the lower frequencies, [0.5, 5] Hz, the amplitude variations are almost identical to the four layer model. At these frequencies the *P*-wave wavelengths are $\gtrsim 350$ m; consequently the waves are only sensitive to long wavelength model features, which are similar across both models to depths of ∼ 400 m (Fig. 7a). At the higher frequencies, [3, 30] Hz, the simulated amplitude reductions (using the Can 2020, model) as a function of distance exhibit similar gradients to the observations for distances < 350 and > 900 m. There is also a small increase (less than a factor of two) in simulated displacements at distances of between 500 and 700 m from the source; however the maximum is not comparable in terms of amplitude or width to the observations. Modelled waveforms indicate that this amplitude increase is due to the positive interference of waves propagating approximately horizontally through the upper ∼ 100 m and refracted arrivals from the positive v_p gradient at depths between 100 and 300 m.

A large suite of models with varying v_p structures were tested to identify a velocity model that can reproduce the observed amplitude variations. Although models employing a smoothly increasing v_p gradient at depths between 100 and 300 m can explain the [3, 30] Hz observations better than the Can (2020) and four-layer models, none of the simulations for which $v_p/v_s \simeq 1.73$ could successfully simulate the observed variations in the [0.5, 5] Hz passband (see Fig. S8 in the Supporting Information for an example of such a model). Improved results are possible if the v_p/v_s ratio is allowed to increase in the upper 150 m of the model (i.e. at depths where we expect to find predominantly alluvium and London Clay, Fig. 2). Previous studies provide a justification for using higher v_p/v_s ratios where such material is expected; measurements of v_p (Conway *et al.* 1984; Hight *et al.* 1997) and v_s (Hight *et al.* 1997; Lessi-Cheimariou *et al.* 2019) are consistent with v_p/v_s ratios greater than five. In addition, simulations of surface waves generated by FSCT also require very low v_s values of < 360 m s^{-1} in the upper 150 m (Read 2024). Fig. 7(c) shows results for our preferred model where the v_p/v_s values reduce from 8.0 to 2.0 over the upper 150 m.

The consequence of increased v_p/v_s ratios is to temporally separate the *P*- and *S*-wave arrivals propagating in the medium, such that *S*-wave arrivals do not interfere with the initial *P*-wave pulses in either passband. This results in the model being able to match the amplitude variations in both passbands, with a source moment of 3×10^{11} N·m. Undertaking a finite-difference simulation using the SW4 package (Petersson *et al.* 2023) utilizing our preferred velocity model (Fig. 7c) provided a complementary visualization of the wavefield evolution. This confirmed that the increased displacement amplitudes between ∼400 and 800 m from the source arise due to the constructive interference of energy propagating almost horizontally through the upper 100 m of the model, and refracted energy returning to the surface from the v_p gradient between 100 and 300 m depth. Supporting Information, including waveforms and wavefield snapshots are provided in Supporting Information Sections H and I.

We recognize that our preferred model is simple, and is unlikely to be a unique solution. We have not, amongst other parameters, considered attenuation (Q) or anisotropy effects upon amplitudes. Additionally, the assumption of a 1-D (depth-dependent) seismic property structure is an approximation; across Foulness Island alluvial deposits are known to infill channels incised into the top of the London Clay (e.g. Lake *et al.* 1986). However, our models demonstrate that the *P*-wave traveltimes and amplitudes are highly dependent upon the subsurface v_p and v_s structure. In particular, the variation in *P*-wave arrival amplitude decay rate as a function of source-to-receiver distance provides a physically justifiable reason for modifying the seismic coupling models of Ford *et al.* (2021).

6 A SEISMIC COUPLING MODEL FOR SATURATED SEDIMENTS

Ford *et al.* (2014) proposed that first-arrival *P*-wave displacements, d (m), generated by near-surface explosions can be predicted from knowledge of the explosive charge mass, W (kg), source-to-receiver distance, r (m), and the HoB of the source, h (m), given the assumption that cube-root (hydrodynamic) scaling holds. Ford *et al.* (2021) developed the following model for seismic displacements,

$$\log\left(\tilde{d}_i\right) = \beta_1 + \beta_2 \log\left(\tilde{r}_{i,j}\right) + \beta_3 \mathsf{logistic}\left(\beta_4 \tilde{h}_j + \beta_5\right) + \epsilon_{i,j} \quad (3)$$

where ϵ is the error vector (assumed to be normally distributed). Natural logarithms are used throughout, and the subscripts refer to the i^{th} station, and j^{th} explosion. The logistic function, $\mathsf{logistic}(\mathsf{x})$, is given by $1/\left(1+e^{-x}\right)$. Recall that the over tilde indicates a parameter that has been scaled by the cube root of the charge mass.

The model (eq. 3) is structured such that β_1 contains information about the shotpoint geological conditions; it is a prediction of the near-source seismic displacement generated by a fully coupled explosion. β_2 describes the decay of signal displacement as a function of distance. The $\beta_3 \mathsf{logistic}\left(\beta_4 \tilde{h}_j + \beta_5\right)$ term models the expected reduction in amplitude as the HoB value increases; β_3 describes the magnitude of the signal amplitude reduction between deeply buried and significantly above-ground explosions, while β_4 and β_5 describe the rate of amplitude decrease as a function of HoB.

β_n are five parameters ($1 \leq n \leq 5$) to be estimated, and Ford *et al.* (2021) showed that the values of β_n depend upon the geological media in, or over, which the explosion has occurred (and in which the seismic waves have propagated). Guided by the data available to them, Ford *et al.* (2021) assumed that β_n do not change as a function of source-to-receiver distance, r. Displacement measurements indicate that this is not the case at Foulness (Fig. 6). Here, we make the assumption that β_m, where $m = 1, 2$ carry information about propagation between source and receiver and will be dependent upon r, but β_p, where $p = 3, 4, 5$ will be a function of shotpoint geology only. Under these assumptions the model (eq. 3) can be updated to,

$$\log\left(\tilde{d}_i\right) = \beta_1\left(r_{i,j}\right) + \beta_2\left(r_{i,j}\right) \log\left(\tilde{r}_{i,j}\right) + \beta_3 \mathsf{logistic}\left(\beta_4 \tilde{h}_j + \beta_5\right) + \epsilon_{i,j} \quad (4)$$

Given the FSCT displacement amplitude observations (Fig. 6), and guided by the modelling results in Section 5, we make the simplifying assumption that at Foulness $\beta_1(r)$ and $\beta_2(r)$ can be considered constant across restricted ranges of source-to-receiver distance where displacement amplitude decay can be approximated by a power-law (i.e. $\tilde{d} \propto \beta_1 \tilde{r}^{\beta_2}$). We note that this complicates the interpretation of the model. An attractive property of the Ford *et al.* (2021) formulation (eq. 3) is that all terms scale hydrodynamically. For the updated model (eq. 4) this is not the case; the amplitude variations are a function of r.

At Foulness we define two distance ranges in which $\beta_m\,(r)$, where $m = 1, 2$, can be considered approximately constant,

$$R_1 = [140, 300]\,\mathrm{m}$$
$$R_2 = [1000, 7000]\,\mathrm{m}$$

The amplitudes in the distance range between R_1 and R_2 (i.e. 300 to 1000 m) exhibit variations that are not consistent with a power-law decay, and are not considered in the simple *P*-wave displacement model constructed here. Numerical modelling results (Section 5) suggest the non power-law amplitude variations are due to the initial *P*-wave in this source-to-receiver distance range being the superposition of direct waves propagating through the upper sediments and arrivals refracted from a v_p gradient at depth.

Due to the higher density of datapoints in R_1 compared to R_2 (Fig. 6) we adopt a two-step procedure to estimate the β parameters. We first undertake a nonlinear least squares inversion, employing a Levenberg–Marquardt algorithm (Newville *et al.* 2023), using only data from distance range R_1 to estimate β_{n,R_1}, where $n = 1, \ldots, 5$. Assuming that $\beta_{p,R_1} = \beta_{p,R_2}$, where $p = 3, 4, 5$ (i.e. the source-dependent terms), we fix β_p and then employ the same nonlinear least squares inversion method using data from distance range R_2 to estimate β_{m,R_2}, where $m = 1, 2$ (i.e. the distance-dependent terms). Estimates of the β parameters, and the associated covariance matrices, are provided in Tables 4 and 5 for the [0.5, 5] Hz passband allowing for direct comparison to the Ford *et al.* (2021) parameters (results for the [3, 30] Hz passband are provided in Tables S3 and S4 in the Supporting Information). Prediction intervals for $\tilde{d}$ are estimated using both the Delta method (e.g. Xu & Long 2005) and a parametric bootstrapping technique. Results from the two methods are broadly similar, so we show only 95 per cent prediction intervals estimated using the Delta method in subsequent plots.

The best-fit model is compared to observations in Fig. 8. For distance range R_1 the logistic curve function (eq. 4) captures the variability in the observations as a function of $\tilde{h}$ (Fig. 8a), with the 95 per cent prediction interval limits for $\tilde{d}$ being a factor of ∼1.7 below and above the mean model at $\tilde{h}$= 0. For explosions close to the surface there is some evidence that a more rapid change occurs in $\tilde{d}$ than can be accommodated by the estimated logistic function; $\tilde{d}$ measurements for S4 ($\tilde{h} = -0.15\,\mathrm{m/kg^{1/3}}$) are higher than the predicted mean model, while $\tilde{d}$ measurements for S5 ($\tilde{h} = 0.03\,\mathrm{m/kg^{1/3}}$) are slightly lower. However, this variability is captured by the prediction interval estimates.

Given the experimental limits on achievable HoB, the data do not fully constrain the logistic curve asymptotes. Despite this, the predicted $\tilde{h}$ values at which full coupling (for negative $\tilde{h}$) and maximum decoupling (for positive $\tilde{h}$) occur are broadly similar to those found by Ford *et al.* (2021). These full coupling and maximum decoupling limits should only be considered valid over a restricted near-surface HoB range (which has yet to be fully determined). For deeply buried explosions the seismic amplitude will decrease due to overburden effects (e.g. Ford & Walter 2013), and for high-altitude bursts no observable *P*-wave displacement from near-epicentre coupling is expected.

The model fit to the observations as a function of source-to-receiver distance confirms that a single power-law amplitude decay with distance is not applicable at Foulness (Fig. 8b). For measurements in the [0.5, 5] Hz passband, the direct wave in the upper geological layers that generates the first arrival across R_1 exhibits a decay parameter $\beta_{2,R_1} = -3.1$, whereas the first arriving refracted arrival in R_2 exhibits a slower decay with distance given by $\beta_{2,R_2} = -2.2$. The sparser data, and larger amplitude variability, in R_2 leads to a wider $\tilde{d}$ prediction interval when compared to R_1: for $\tilde{h} = -0.3\ \mathrm{m/kg^{1/3}}$ the ratio of the upper to lower 95 per cent prediction interval limits is 2.9 in R_1 (at $\tilde{r} = 40\ \mathrm{m/kg^{1/3}}$) whereas it equals 4.2 in R_2 (at $\tilde{r} = 300\,\mathrm{m/kg^{1/3}}$).

The model variations as a function of HoB are qualitatively similar across the FSCT and Ford *et al.* (2021) geological settings (Fig. 9); the most rapid reductions in $\tilde{d}$ are predicted as the HoB increases from a burial of $\tilde{h} \sim -0.5\ \mathrm{m/kg^{1/3}}$ to a height of $\tilde{h} \sim 0.3\ \mathrm{m/kg^{1/3}}$ (Figs 9a & b). However, the change in $\tilde{d}$ between fully coupled (deeply buried) explosions and detonations at, or above, the surface is highly dependent upon geology, as found by Ford *et al.* (2021). Recognizing that $\tilde{d} = \tilde{d}\left(\tilde{h}, \tilde{r}, r\right)$ (eq. 4), a predicted decoupling factor, $\gamma\left(\tilde{h}\right)$, can be defined as,

$$\gamma\left(\tilde{h}\right) = \frac{\tilde{d}\,(-2, \tilde{r}, r)}{\tilde{d}\left(\tilde{h}, \tilde{r}, r\right)} \tag{5}$$

and represents the reduction in scaled displacement in comparison to a fully coupled, deeply buried, explosion. Decoupling factors for surface explosions, $\gamma\,(0)$, and example above-ground explosions, $\gamma\,(1)$, are given in Table 6; these suggest that saturated ground conditions, such as the wet estuarine sediments at Foulness (Section 3) and those constraining the wet-rock model of Ford *et al.* (2021), lead to higher variations in near-surface coupling than soft or hard dry rock. For example, the surface explosion decoupling factor, $\gamma\,(0)$, at Foulness is estimated to be 22, compared to the soft-rock model of Ford *et al.* (2021) for which $\gamma\,(0) = 2.3$.

The absolute value of $\tilde{d}$ at a given $\tilde{h}$ (and the relative value compared to other geologies) is highly dependent upon the distance (i.e. $\tilde{r}$) at which the measurement is made. This is particularly pronounced when comparing FSCT results with those from Ford *et al.* (2021) due to the difference in amplitude decay with distance in the models, as captured by parameter β_2 (e.g. Figs 9c & d). At Foulness $\beta_2 = -2.2$ at $\tilde{r} \geq 200\ \mathrm{m/kg^{1/3}}$, whereas the three Ford *et al.* (2021) models have β_2 values between −1.1 and −1.3. Consequently, at short stand-off distances from an explosion (e.g. $\tilde{r} = 220\ \mathrm{m/kg^{1/3}}$) the FSCT model predicts $\tilde{d}$ at $\tilde{h}$= 0 that are a factor of 4.4 greater than the Ford *et al.* (2021) wet-rock model (Fig. 9a), but as $\tilde{r}$ increases to 800 $\mathrm{m/kg^{1/3}}$ the difference between the predicted $\tilde{d}$ for surface explosions reduces to ∼15 per cent (Fig. 9b). At further distances the predicted $\tilde{d}$ for Foulness conditions will become lower than those predicted by the Ford *et al.* (2021) models.

Although the difference in β_2 values between this study and Ford *et al.* (2021) is large, numerical modelling of the initial *P*-wave phases at Foulness (Section 5 and Fig. 7) show amplitude decay rates with distance that are consistent with β_2 values ≤ -2. The difference between the FSCT and Ford *et al.* (2021) β_2 values is discussed in Section 7.

7 DISCUSSION

The FSCT explosions occurred within, or above, soft saturated estuarine sediments. The measured PPV decay with distance at Foulness (Fig. 3) confirms that the propagation conditions close to the source ($\tilde{r} < 40\ \mathrm{m/kg^{1/3}}$) are consistent with previous ground shock studies in saturated sandy clays (Department of the Army 1986, TM 5-855-1). Therefore, we are confident that the FSCT provide results that are complementary to recently developed models of seismic coupling as a function of HoB in hard rock, soft rock and wet (water) environments (Ford *et al.* 2021). A comparison of the FSCT results with the models in other geological settings can be divided

Table 4. Least-squares estimates of the *P*-wave displacement model parameters (β_n, where $n = 1, \ldots, 5$, eq. 4) and the associated covariance matrix, for observations in the [0.5, 5] Hz passband and the [150, 300] m source-to-receiver distance range (R_1).

Parameter		β_1	β_2	β_3	β_4	β_5
Mean value		0.04	−3.07	−4.99	3.17	0.48
	β_1	0.25	−0.045	−0.16	−0.14	−0.022
	β_2	−0.045	0.0084	0.025	0.020	0.0026
Covariance	β_3	−0.16	0.025	0.19	0.16	0.047
	β_4	−0.14	0.020	0.16	0.14	0.040
	β_5	−0.022	0.0026	0.047	0.040	0.017

Table 5. Least-squares estimates of the *P*-wave displacement model parameters (β_m, where $m = 1, 2$, eq. 4) and the associated covariance matrix, for observations in the [0.5, 5] Hz passband and the [1000, 7000] m source-to-receiver distance range (R_2). β_p, where $p = 3, 4, 5$, are assumed to take the same values as the inversion undertaken at closer source-to-receiver distances (Table 4).

Parameter		β_1	β_2
Mean value		−2.17	−2.16
Covariance	β_1	1.1	−0.19
	β_2	−0.19	0.032

into two components: the effects of near-source coupling and local seismic propagation.

7.1 Near-source coupling effects

The near-source coupling effects can be posed as two inter-related questions: (1) What is the predicted seismic displacement for a fully coupled (i.e. deeply buried) explosion, and (2) what is the expected reduction in displacement as the HoB of the explosion increases?

7.1.1 Estimated displacements for fully coupled explosions

In eq. (4), information regarding the near-field displacements expected for a fully coupled source is captured by β_1. Comparing β_1 values for FSCT (β_{1,R_1} =0.04) and the Ford *et al.* (2021) models ($-11.4 < \beta_1 < -9.6$) indicates very large differences between the expected displacements in the [0.5, 5] Hz passband at $\tilde{r} = 1$ m/kg$^{1/3}$. However, because the seismic measurements are restricted to $\tilde{r} > 30$ m/kg$^{1/3}$, the β_1 values are highly sensitive to the estimate of parameter β_2: the rate of *P*-wave displacement reduction with distance. As noted in Section 6 the β_2 values in Ford *et al.* (2021) ($-1.3 < \beta_2 < -1.1$) are considerably less than those identified for Foulness ($\beta_{2,R_1} = -3.07$, $\beta_{2,R_2} = -2.16$), consistent with lower β_1 values for the Ford *et al.* (2021) model (see e.g. Figs 9c and d). The data slices shown by Ford *et al.* (2021) illustrating displacement reduction with distance (their fig. 13, upper right panel) do not, in our opinion, provide a good fit between model and data for the soft- and wet-rock models. In both cases, the reduction in *P*-wave displacement measurements with distance appears more rapid than the model predicts. This is consistent with earlier studies using the data; the original soft-rock model of Ford *et al.* (2014) found $\beta_2 = -1.74$, and the re-analysis of Templeton *et al.* (2018) gave an alluvium model $\beta_2 = -1.87 \pm 0.18$.

The mismatch between model and data amplitude decay with distance is particularly notable for the wet-rock model of Ford *et al.* (2021); the data point at $\tilde{r} = 100$ m/kg$^{1/3}$ that has an amplitude of ~ 30 nm/kg$^{1/3}$ has a displacement almost two standard deviations above the median model prediction (fig. 13 of Ford *et al.* 2021). We note that FSCT displacements at similar scaled distances, which are at distances just less than those influenced by velocity gradients at depth (see Section 5), have almost identical amplitudes (~ 30 nm/kg$^{1/3}$, Fig. 6c). The wet model of Ford *et al.* (2021) was constrained using data from a series of explosions at Aberdeen Proving Ground, Maryland, US (the Humming Terrapin trials, see e.g. Stone 2017), where Precambrian metamorphic basement rocks are overlain by between 20 and 90 m of water-saturated clays, gravels and sands (Whitten *et al.* 1997). We might therefore expect qualitatively similar propagation conditions for Humming Terrapin and FSCT. A future joint re-analysis of these two data sets may provide insight into whether unmodelled refraction effects should be taken into account for the Ford *et al.* (2021) wet model, leading to revised β_1 and β_2 estimates. To summarize, it is currently difficult to compare the near-source predicted seismic amplitudes for this study and those of Ford *et al.* (2021) due to the large variation in amplitude decay predictions.

7.1.2 The effect of HoB on seismic coupling

The predicted reduction in displacement as a function of increasing HoB has shown to be larger for saturated sediments (FSCT) and the Ford *et al.* (2021) wet-rock model when compared to (dry) soft or hard rocks (e.g. Fig. 9). The reduction in coupling for a surface explosion when compared to a deeply-buried explosion is predicted to be almost ten times larger in saturated sediments when compared to the dry alluvium underpinning the Ford *et al.* (2021) soft rock model (Table 6). Increased coupling for deeply-buried explosions in water and clays (Fig. 9) is consistent with observations of underground nuclear tests in different geological media (Murphy 1996), the high seismic efficiency of underwater chemical explosions (e.g. Khalturin *et al.* 1998), and exploration geophysics practices of setting charges below the water table and in clays to increase explosive effectiveness (e.g. Section 7.2, Sheriff & Geldart 1995).

Although the magnitude of predicted displacement reductions as HoB increases is dependent upon the geological setting, the scaled HoB at which decoupling occurs is less variable. The $\tilde{h}$ value at which half the full decoupling in log displacement is achieved (indicated by the ratio $-\beta_5/\beta_4$, eq. 4) is always at shallow below-ground burial depths, ranging between −0.15 to −0.03 m/kg$^{1/3}$ across the four models.

Despite the model uncertainties being highly dependent upon r, $\tilde{r}$, $\tilde{h}$ and geological setting (e.g. Fig. 9), it is instructive to look at an example to illustrate the uncertainties in yield inference associated with seismic-only models. For a station at 1665 m from a 100 kg surface explosion the mean model displacement prediction, $\bar{d}$, in

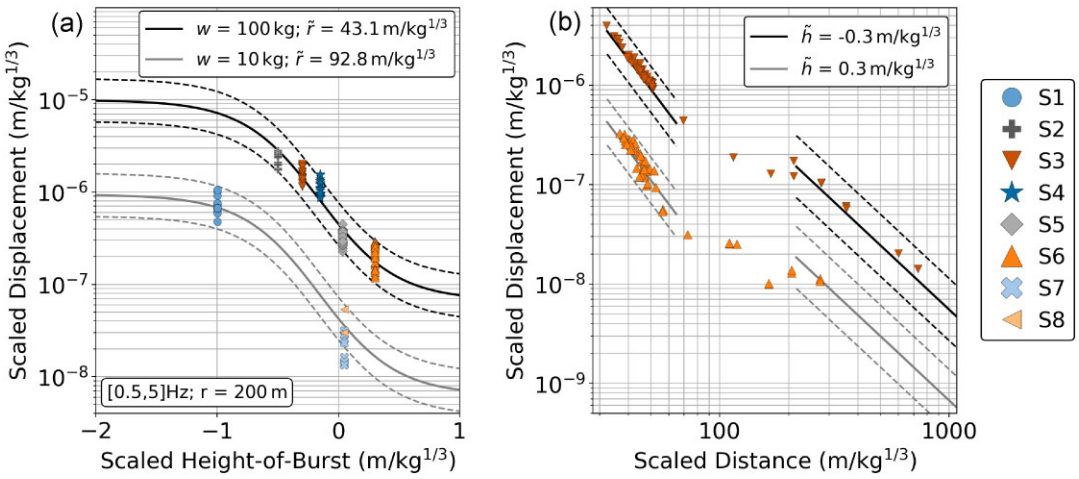

Figure 8. The scaled seismic displacement model (eq. 4) fit to the measured FSCT amplitudes in the [0.5, 5] Hz passband, as a function of scaled HoB (panel a) and scaled distance (panel b). Variations with HoB (panel a) are shown at $r = 200$ m, within a distance range for which there is a high density of geophone recordings (Figs 1b and 6). The superimposed measured amplitudes (coloured symbols) are taken from the [180, 220] m distance range. Two models are shown, corresponding to the scaled distances of the 100 kg explosions (black lines) and the 10 kg explosions (grey lines). The solid lines are the mean model, with the dashed lines representing the 95 per cent prediction interval. Variations with scaled distance (panel b) are shown for a below ground explosion (S3, $\tilde{h}=-0.3$ m/kg$^{1/3}$) and an above ground explosion (S6, $\tilde{h}=0.3$ m/kg$^{1/3}$); the models are only shown across the scaled distances for which they were calculated.

the 0.5 to 5 Hz passband is 73 nm, with an associated 95 per cent prediction interval spanning [36, 150] nm. The equivalent experimental measurement (station TR07, shot S5) is 54 nm. The prediction interval is approximately $[\bar{d}/2, 2\bar{d}]$; utilizing the cube-root scaling assumption this displacement interval is equivalent to an interval of $[\bar{w}/8, 8\bar{w}]$ where $\bar{w}$ is the yield estimated from $\bar{d}$. This large yield uncertainty demonstrates the difficulty in using seismic-only models for near-surface explosion yield inference, and the need for complementary models using other data sources to constrain the estimate (e.g. airblast impulse, Ford *et al.* 2021). In addition, we have considered a case where an appropriate geological model has been chosen by the analyst. If an incorrect model was chosen, for example, if the soft rock model was used to interpret data from a saturated sediment environment, the results would be subject to a significant bias (e.g. Fig. 9).

7.2 Local propagation effects

When considering the effects of local propagation upon explosively generated seismic *P*-waves, FSCT provides an example where seismic velocity contrasts at depth lead to changes in the propagation path taken by the initial *P*-wave with increasing source-to-receiver distance. At short source-to-receiver distances the initial *P*-wave is a direct arrival within the near-surface sediments. As the source-to-receiver distance increases the initial *P*-wave is associated with arrivals refracted from velocity gradients at depth (e.g. Figs 5 and 6). A consequence of this is that models of the initial *P*-wave displacement (e.g. eqs 3 and 4) cannot be a function of the explosion site near-surface geology alone; knowledge of the deeper geology is required. Depths to refractors control the source-to-receiver distance at which particular propagation dependent parameters (β_1, β_2) will be applicable, and presumably the material properties of the deeper layers (and the impedence contrasts between the layers) will affect the absolute amplitudes of the refracted arrivals.

The FSCT results provide an example where complex amplitude variations with distance can occur; we interpret an amplitude increase with increasing distance from the source as being generated by superposition of direct waves and refracted waves. At Foulness the observations suggest positive velocity gradients at depth enhance these amplitude variations, although such interference patterns are also possible in simple layered structures (e.g. Červený 1966). These observations have implications for the transportability of models for interpreting explosively generated *P*-wave displacements at local distances.

At distances > 1000 m, the FSCT seismometer network has a restricted azimuthal coverage of 54° (Fig. 1), such that the model (Section 6) will not capture any azimuthal *P*-wave amplitude variations resulting from subsurface structure towards the south and west. However, our measurements can be satisfactorily modelled using a sequence of horizontal layers, in agreement with previous geological interpretations (see Section 3). At other locations 3-D subsurface structural features may lead to more complex *P*-wave amplitude variations that depend both on range and azimuth.

The trials described by Ford *et al.* (2014) and this study (FSCT) were designed with the purpose of constraining model parameters that could then be applied to rapid post-event analysis of seismic data from explosions in locations with similar near-surface rocks or soils. The FSCT results suggest that caution will be required when applying these models to geographical areas for which validated models are not available.

Due to the increasing density of seismometer networks, seismological studies of accidental or terrorist explosions occasionally have a small number of recordings at distances < 10 km, (e.g. Koper *et al.* 1999; Zhao *et al.* 2016) for which relationships such as those developed in Ford *et al.* (2021) and this study may be applicable for explosive yield estimation. However, it is perhaps more common for seismological investigations of explosions to only have access to recordings at distances at tens of kilometres, or further, from the detonation (e.g. Pilger *et al.* 2021; Song *et al.* 2022; Nippress *et al.* 2023). In these cases one might calculate a seismic magnitude and utilize an appropriate magnitude-to-yield relationship (validated for fully coupled explosions) to which a decoupling factor can be applied to account for the explosion being close to the surface (see

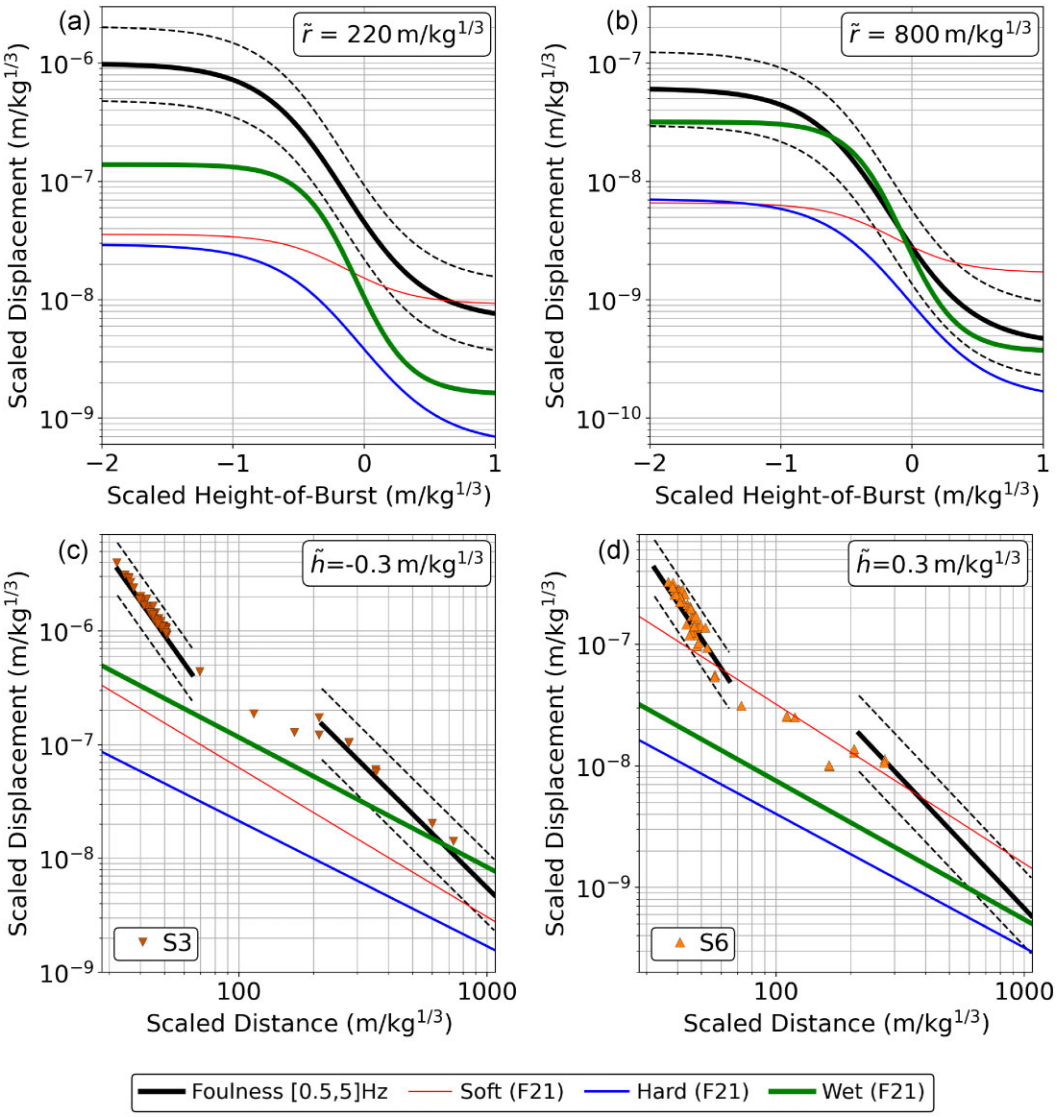

Figure 9. Comparison of the FSCT seismic displacement model (black lines) with those reported for different geological settings by Ford *et al.* (2021), indicated as F21 in the legend. All models are for [0.5, 5] Hz passband predictions. The model variations as a function of scaled HoB are shown at scaled distances of 220 m/kg$^{1/3}$ (panel a) for comparison with Ford *et al.* (2021) and at 800 m/kg$^{1/3}$ (panel b) to illustrate the difference in scaled displacements at different distances from an explosion. Modelled scaled displacements as a function of scaled distance for an above-ground explosion (panel c) and a below-ground explosion (panel d) show the difference in scaled displacement amplitude for explosions at different scaled HoB. Solid lines indicate the mean model; dashed lines for the FSCT models indicate the 95 per cent prediction interval. In panels (c) and (d), an explosive charge mass of 100 kg was assumed when calculating the scaled distance ranges at which the FSCT models were applicable, such that the S3 and S6 data (symbols) could be added for direct comparison.

Table 6. Predicted decoupling factors $\gamma\left(\tilde{h}\right)$ (eq. 5) for surface, $\left(\tilde{h}=0\right)$, and above-ground, $\left(\tilde{h}=1\right)$, explosions.

Model		γ (0)	γ (1)
	Soft	2.3	3.8
Ford *et al.* (2021)	Hard	7.6	42
	Wet	13	85
FSCT (this study)		22	130

e.g. Khalturin *et al.* 1998). As the decoupling factors estimated in experiments such as FSCT (e.g. Table 6) are only dependent upon the source geology and explosive height-of-burst, they may be suitable for wider application within magnitude-to-yield relationships. However, many regional magnitude scales are not based upon *P*-wave displacements, and the applicability of *P*-wave decoupling factors to other phases (e.g. L_g) has not been verified. A further complication is that where local and regional *P*-wave magnitude scales exist (e.g. Green *et al.* 2020) there are not always well constrained magnitude-to-yield relationships available for fully coupled explosions.

8 FUTURE STUDIES

Seismic propagation within layered geologies leads to complex variations in *P*-wave amplitudes as a function of distance from the source. In such settings where there are not significant lateral variations in seismic properties (e.g. Foulness), surface wave amplitudes

may exhibit a simpler decay relationship as a function of distance (e.g. Bonner *et al.* 2013b; Read 2024). Such a scenario may allow a site-specific empirical relationship, of the form proposed by Ford *et al.* (2021), to be developed linking charge mass, source-to-receiver distance, and HOB to surface wave amplitude. Such a relationship would have the advantage that hydrodynamic scaling laws would be applicable across all distances, although the effects of along-path attenuation (Q) may have to be accounted for. Testing whether such a relationship exists for the FSCT surface wave recordings will motivate a future study.

A comprehensive analysis of FSCT high-speed video and laser scan data would also be beneficial, as it would likely provide constraints on crater formation processes. Crater dimensions may provide additional constraints for explosive charge mass estimation routines (e.g. Cooper 1976), and an understanding of the time- and length-scales of crater formation will be of interest when considering the seismic surface wave source function for near-surface explosions.

9 CONCLUDING REMARKS

Ground motion data from the eight explosions comprising FSCT provide insight into seismoacoustic energy partitioning for near-surface explosions in, and above, saturated sediments. Measurements of peak particle velocities within 100 m of the explosions are consistent with previous ground shock measurements in saturated clays.

At Foulness, the initial *P*-wave displacement amplitudes display complex variations as a function of distance away from the source, exhibiting both distance-dependent variations in the rate of decay and a distance range in which amplitudes increase to a local maximum. Numerical modelling suggests that both effects can be explained by the layered geology beneath Foulness. Seismic multipathing causes the initial *P*-wave to be associated with distinct paths (direct waves, refracted arrivals) within distinct ranges of source-to-receiver distance, with each propagation path exhibiting a different amplitude decay rate as a function of distance. The observed local maximum in initial *P*-wave amplitude between 700 and 1000 m from the source is shown to be the result of constructive interference, between waves propagating through the upper sediments and waves propagating along longer, faster paths that return from velocity gradients at depth. The observation of this amplitude maximum at short stand-off distances from the explosion appears to be associated with the high v_p/v_s ratios (i.e. values >5) expected for saturated London Clays. Simulations suggest that, in settings where $v_p/v_s \simeq 1.73$, the interference between *P*- and *S*-waves in the [0.5, 5] Hz passband at short stand-off distances would cause truncation of the *P*-wave pulse, such that the amplitude maximum would not be observed.

An aim of seismoacoustic partitioning studies is to provide simplified models for predicting *P*-wave displacements given knowledge of the explosive yield, source height-of-burst, source-to-receiver distance and near-source geological setting. To account for the observed distance-dependent effects in the FSCT data set, we have proposed a model that extends the formulation developed by Ford *et al.* (2021). This updated model allows for distance-dependence by defining discrete distance ranges in which the amplitude decay with distance can be approximated by a power-law decay. Model parameters associated with the source height-of-burst remain independent of the source-to-receiver distance. At Foulness deeply-buried explosions produced near-source seismic amplitudes over an order-of-magnitude larger than those expected for sources in hard rock and dry alluvium. Additionally, the reduction in *P*-wave displacement for a surface explosion, compared to a tamped explosion, is approximately a factor of 20 for seismic signals in the [0.5, 5] Hz passband; this is almost ten times larger than models for dry alluvium (Ford *et al.* 2021).

Explaining the *P*-wave displacement variations as a function of source-to-receiver distance at Foulness required a detailed understanding of the geological structure, and associated geophysical parameters, beneath the source region. This was aided by previous geological interpretations of borehole logs (e.g. Lake *et al.* 1986), targeted geophysical surveys (e.g. Can 2020) and knowledge of wave propagation in similar environments (e.g. Lessi-Cheimariou *et al.* 2019). Given the difference in both amplitude decay and height-of-burst variations compared to results from other trials (e.g. Ford *et al.* 2021), this raises questions regarding the transportability of empirically derived *P*-wave amplitude relationships. In limited circumstances, numerical modelling results may be able to guide an analyst. For instance, if an explosion occurred within similar media to an existing model, but at a location with different thicknesses of geological units, modelling results may help to identify distance ranges where empirical models remain applicable. However, when faced with determining the correct model for a locality where little is known about the subsurface structure, care will need to be taken to address the uncertainties related to transporting the empirical relationships.

ACKNOWLEDGMENTS

We thank Sean Ford, an anonymous reviewer, and our editor, Anne Obermann, for their insightful comments that improved earlier versions of this manuscript.

We thank representatives from the UK Ministry of Defence, QinetiQ, AWE and Spurpark Ltd. whose expertize and commitment ensured the successful firing of the Foulness Seismoacoustic Coupling Trials. Technical field support and logistics were provided by Spurpark Ltd, and Andrew Pretorius, University of Leeds. Colleagues at AWE Blacknest, in particular Sheila Peacock, are thanked for data management assistance.

We thank Prof. Graham Stuart, Samuel Greenwood and James Ward for their participation in pre-trial geophysical surveys conducted by the University of Leeds.

AN was funded by NERC (REMIS: Reliable Earthquake Magnitudes for Induced Seismicity, NE/R001154/1; MC^2: Mantle Circulation Constrained, NE/T012684/1), JW and NT were funded by UK Science and Technology Facilities Council grant ST/W002523/1.

AUTHOR CONTRIBUTIONS

DNG & SEJN identified the overarching research need. DNG, SEJN, RAC, CT, AN & BS worked together to develop the trials and data collection methodology. DNG, SEJN, AN, CT & BS were part of the team that undertook the data collection in the field during the FSCT trials, with SdR providing access to extra sensors. CT provided trials leadership and supervision. RAC & SEJN undertook pre-trial surveys, and TCP analysed the resulting data. DNG, SEJN, ER, NB, JW & NAT contributed to signal analysis, software development and numerical modelling efforts. AN & DNG coordinated the data curation activities. DNG wrote the original manuscript draft; all authors contributed to reviewing & editing.

SUPPORTING INFORMATION

Supplementary data are available at *GJIRAS* online.

suppl_data

Please note: Oxford University Press is not responsible for the content or functionality of any supporting materials supplied by the authors. Any queries (other than missing material) should be directed to the corresponding author for the paper.

DATA AVAILABILITY

Borehole records can be found within the British Geological Survey's National Geoscience Data Centres collection: https://www.bgs.ac.uk/information-hub/borehole-records/

From mid-2025 all seismic data will be available via the EarthScope Consortium Web Services (https://service.iris.edu/), stored with the following seismic network reference: 5F, Green & Nowacki (2021), or upon reasonable request to the corresponding author (dgreen@blacknest.gov.uk).

REFERENCES

Banda, E., Deichmann, N., Braile, L.W. & Ansorge, J., 1982. Amplitude study of the P_g phase, *J. Geophys.,* **51,** 153–164.

Bell, F.G., Culshaw, M.G. & Cripps, J.C., 1999. A review of selected engineering geological characteristics of English Chalk, *Eng. Geol.,* **54**(3–4), 237–269.

Bonner, J., Waxler, R., Gitterman, Y. & Hofstetter, R., 2013a. Seismoacoustic energy partitioning at near-source and local distances from the 2011 Sayarim explosions in the Negev Desert, Israel, *Bull. seism. Soc. Am.,* **103**(2A), 741–758.

Bonner, J.L., Russell, D.R. & Reinke, R.E., 2013b. Modelling surface waves from aboveground and underground explosions in Alluvium and Limestone, *Bull. seism. Soc. Am.,* **103**(6), 2953–2970.

Boshier, R.E., 1982. *AWRE Foulness Underwater Range*. Tech. Rep. FGE/1552, Foundation and Ground Engineering Branch, Directorate of Civil Engineering Services, Department of the Environment.

Boshier, R.E., 1983. *Foulness Island, Atomic Weapons Establishment 200 Metre Small Calibre Range (C4)*. Tech. Rep. FGE/1827, Foundation and Ground Engineering Branch, Directorate of Civil Engineering Services, Department of the Environment.

Can, T., 2020. *Reprocessing of a 2D Seismic Line in Foulness Island, UK, to Derive a High-Resolution Subsurface Velocity Model. Unpublished MSc Exploration Geophysics Dissertation,* School of Earth and Environment, University of Leeds, Leeds, UK.

Červený, V., 1966. On dynamic properties of reflected and head waves in the n-layered Earth's crust, *Geophys. J. R. Astron. Soc.,* **11**(1), 139–147.

Collins, A., 2018. Site characterisation of seismic wave speeds of quaternary and tertiary overburden and underlying cretaceous chalk, Foulness Island, *Unpublished MSc Exploration Geophysics Dissertation,* School of Earth and Environment, University of Leeds, Leeds, UK.

Conway, B.W., McCann, D.M., Sarginson, M. & Floyd, R.A., 1984. A geophysical survey of the Crouch/Roach river system in South Essex with special reference to buried channels, *Q. J. Eng. Geol. London,* **17,** 269–282.

Cooper, H.F., 1976. *Estimates of Crater Dimensions for Near-Surface Explosions of Nuclear and High-Explosive Sources,* Tech. rep., R & D Associates, RDA-TR-2604-001.

Department of the Army, 1986. *Fundamentals of Protective Design for Conventional Weapons*. Technical Manual TM 5-855-1, Department of the Army, Washington, DC, USA.

Denny, M.D. & Johnson, L.R., 1991. The explosion seismic source function: models and scaling laws reviewed, *Explosion Source Phenomenology,* pp. 1–24, eds, Taylor, S.R., Patton, H.J. & Richards, PG., American Geophysical Union, Washington, DC doi:10.1029/GM065p0001.

Douglas, A. & Marshall, P.D., 1996. Seismic source size and yield for nuclear explosions, *Monitoring a Comprehensive Test Ban Treaty,* pp. 225–245, eds, Husebye, E. & Dainty, A., Kluwer Academic Press, Dordrecht doi:10.1007/978-94-011-0419-7_19.

Drake, J.L. & Little, C.D., 1983. Ground shock from penetrating conventional weapons, In *Proceedings of the Interaction of Non-Nuclear Munitions with Structures, U.S,* pp. 1–6, Air Force Academy, Colorado.

Ford, S.R. & Vorobiev, O.Y., 2023. Numerical modelling of air-blast suppression as a function of explosive-charge burial depth, *Bull. seism. Soc. Am.,* **113**(4), 1628–1634.

Ford, S.R. & Walter, W.R., 2013. An explosion model comparison with insights from the source physics experiments, *Bull. seism. Soc. Am.,* **103**(5), 2937–2945.

Ford, S.R., Rodgers, A.J., Xu, H., Templeton, D.C., Harben, P., Foxall, W. & Reinke, R.E., 2014. Partitioning of seismoacoustic energy and estimation of yield and height-of-burst/depth-of-burial for near-surface explosions, *Bull. seism. Soc. Am.,* **104**(2), 608–623.

Ford, S.R., Bulaevskaya, V., Ramirez, A., Johannesson, G. & Rodgers, A.J., 2021. Joint Bayesian inference for near-surface explosion yield and height-of-burst, *J. Geophys. Res. Solid Earth,* **126**(2), e2020JB020968 doi:10.1029/2020JB020968.

Green, D. & Nowacki, A., 2021. *Foulness Seismoacoustic Coupling Trial* Dataset, doi:10.7914/SN/5F_2021.

Green, D.N., Luckett, R., Baptie, B. & Bowers, D., 2020. A UK local seismic magnitude scale, ML^P, using *P*-wave amplitudes, *Geophys. J. Int.,* **223**(3), 2054–2065.

Herrmann, R.B., 2013. Computer programs in seismology: an evolving tool for instruction and research, *Seism. Res. Lett.,* **84**(6), 1081–1088.

Hight, D.W., Bennell, J.D., Chana, B., Davis, P.D., Jardine, R.J. & Porovic, E., 1997. Wave velocity and stiffness measurements of the Crag and Lower London tertiaries at sizewell, *Géotechnique,* **47**(3), 451–474.

Jardetzky, W.S. & Press, F., 1952. Rayleigh-wave coupling to atmospheric compression waves, *Bull. seism. Soc. Am.,* **42**(2), 135–144.

Khalturin, V.I., Rautian, T.G. & Richards, P.G., 1998. The seismic signal strength of chemical explosions, *Bull. seism. Soc. Am.,* **88**(6), 1511–1524.

Kim, K. & Pasyanos, M.E., 2023. Seismoacoustic explosion yield and depth estimation: insights from the large surface explosion coupling experiment, *Bull. seism. Soc. Am.,* **113**(4), 1457–1470.

Kinney, G.F. & Graham, K.J., 1985. *Explosive Shocks in Air,* 2nd edn., Springer-Verlag, Berlin.

Koper, K.D., Wallace, T.C. & Hollnack, D., 1999. Seismic analysis of the 7 August 1998 truck-bomb blast at the American Embassy in Nairobi, Kenya, *Seism. Res. Lett.,* **70**(5), 512–521.

Koper, K.D., Wallace, T.C., Reinke, R.E. & Leverette, J.A., 2002. Empirical scaling laws from truck bomb explosions based on seismic and acoustic data, *Bull. seism. Soc. Am.,* **92**(2), 527–542.

Lake, R., Ellison, R., Hanson, M. & Conway, B., 1986. *Geology of the Country Around Southend and Foulness, Memoir for, 1,50000 sheets 258 and 259,* Tech. rep., British Geological Survey, London

Langston, C.A., 2004. Seismic ground motions from a Bolide shock wave, *J. geophys. Res.,* **109**(B12309) doi:10.1029/2004JB003167.

Lessi-Cheimariou, A., Tromans, I., Hadlow, N., Floyd, M. & Pateman, J., 2019. A novel technique for deep seismic cone tests in challenging ground conditions, In *Proceedings of SECED Conference 2019: Earthquake Risk and Engineering Towards a Resilient World, Greenwich,* Society for Earthquake and Civil Engineering Dynamics, pp. 1–10.

Murphy, J.R., 1996. Types of seismic events and their source description, In *Monitoring a Comprehensive Test Ban Treaty,* eds, Husebye, E. & Dainty, A., Kluwer Academic Press, Dordrecht doi:10.1007/978-94-011-0419-7_16.

Newville, M. *et al.*, 2023. *LMFIT: Non-Linear Least-Square Minimization and Curve-Fitting for Python (1.2.2),* Zenodo doi:10.5281/zenodo.8145703.

Nippress, S.E.J., Nippress, A. & Green, D.N., 2023. Seismoacoustic analysis of the 7 July 2011 Abadan, Turkmenistan, explosions, *Bull. seism. Soc. Am.,* **113**(4), 1635–1651.

Nishimura, S., Jardine, R. & Minh, N., 2007. Shear strength anisotropy of natural London clay, *Geotechnique,* **57**(1), 49–62

Pasyanos, M.E. & Ford, S.R., 2015. Determining the source characteristics of explosions near the Earth's surface, *Geophys. Res. Lett.,* **42**(10), 3786–3792.

Petersson, N.A., Sjögreen, B., Tang, H. & Pankajakshan, R., 2023. *geodynamics/sw4: Sw4, version 3.0,* 10.5281/zenodo.8322590.

Pilger, C., Gaebler, P., Hupe, P., Kalia, A.C., Schneider, F.M., Steinberg, A., Sudhaus, H. & Ceranna, L., 2021. Yield estimation of the 2020 Beirut explosion using open access waveform and remote sensing data, *Sci. Rep.,* **11**(1), 14 144.

Read, E., 2024. Seismic coupling of surface waves in clay sediments from subsurface and subaerial explosions *Masters Research Thesis,* School of Earth Sciences, University of Bristol, Bristol, UK.

Shelton, T.W., Ehrgott, J.Q., Jr., Moral, R.J. & Barbato, M., 2014. Experimental and numerical investigations of the ground shock coupling factor for near-surface detonations, *Shock and Vibration,* **2014**(789202), 1–11.

Sheriff, R.E. & Geldart, L.P., 1995. *Exploration Seismology,* 2nd edn., Cambridge University Press.

Smart, J.GO., Sabine, P.A. & Bullerwell, W., 1964. The geological survey exploratory borehole at Canvey Island, Essex, *Bull. Geol. Surv., Great Britain,* **21,** 1–36.

Song, Y., Zhao, L.F., Xie, X.B., Ma, X., Du, G., Tian, X. & Yao, Z.X., 2022. Seismological observations on the 2019 March 21 accidental explosion at Xiangshui chemical plant in Jiangsu, China, *Geophys. J. Int.,* **228**(1), 538–550.

Stone, R., 2017. Test blasts simulate a nuclear attack on a port, *Science,* **355**(6328), 897 doi:10.1126/science.aal0839.

Sumbler, M.G., 1996. *British Regional Geology: London and the Thames Valley,* 4th edn., HMSO for the British Geological Survey, London.

Templeton, D.C., Rodgers, A.J., Ford, S.R., Harben, P.E., Ramirez, A.L., Foxall, W. & Reinke, R.E., 2018. Seismic models for near-surface explosion yield estimation in alluvium and sedimentary rock, *Bull. seism. Soc. Am.,* **108**(3A), 1384–1398.

Whitten, C.B., Swartzel, S.M., Miller, S.P. & Blough, K., 1997. *Conceptual Hydrogeologic Model of Aberdeen Proving Ground - Aberdeen Area,* Tech. rep., US Army Corps of Engineers, Waterways Experiment Station , Report GL-97-16.

Williams, B.J. *et al.*, 2021. Multiphenomenology explosion monitoring (MultiPEM): a general framework for data interpretation and yield estimation, *Geophys. J. Int.,* **226**(1), 14–32.

Wills, G., Nippress, A., Green, D.N. & Spence, P.J., 2022. Site-specific variations in air-to-ground coupled seismic arrivals from the 2012 October 16 explosion at Camp Minden, Louisiana, United States, *Geophys. J. Int.,* **231**(1), 243–255.

Xu, J. & Long, J.S., 2005. Confidence intervals for predicted outcomes in regression models for categorical outcomes, *The Stata J.,* **5**(4), 537–539.

Zhao, X. *et al.*, 2016. Seismological investigations of two massive explosions in Tianjin, China, *Seism. Res. Lett.,* **87**(4), 826–836.